

Title:

The Ediacaran ‘Miaohe Member’ of South China: new insights from paleoredox proxies and stable isotope data

Category: The Ediacaran System and the Ediacaran-Cambrian Transition

Authors:

Paul Bridger^{1,3}, Simon W. Poulton², Ying Zhou³, Chao Li⁴, Kun Zhang³, Graham A. Shields³

Affiliations:

¹British Geological Survey, Nicker Hill, Keyworth, Nottingham, NG12 5GG, UK (email: pbr@bgs.ac.uk)

²School of Earth and Environment, University of Leeds, Leeds LS2 9JT, UK

³Department of Earth Sciences, University College London, Gower Street, London WC1E 6BT, UK

⁴State Key Laboratory of Biogeology and Environmental Geology, China University of Geosciences, Wuhan, 430074, China

Keywords:

Doushantuo Formation, iron speciation, redox-sensitive trace metals, nitrogen isotopes, carbon isotopes, chemostratigraphy

Abstract

Throughout the Ediacaran Period, variable water-column redox conditions persisted along productive ocean margins due to a complex interplay between nutrient supply and oceanographic restriction. These changing conditions are considered to have influenced early faunal evolution, with marine anoxia potentially inhibiting the development of the ecological niches necessary for aerobic life forms. To understand this link between oxygenation and evolution, the combined geochemical and paleontological study of marine sediments is preferable. Located in the Yangtze Gorges region of southern China, lagoonal black shales at Miaohe preserve alga and putative metazoans, including *Eoandromeda*, a candidate total-group ctenophore, thereby providing one example of where integrated study is possible. Presented herein, is a multi-proxy investigation into water-column redox variability during deposition of these shales (c. 560 to 551 Ma). For this interval, reactive iron partitioning indicates persistent water-column anoxia, while trace metal enrichments and other geochemical data suggest temporal fluctuations between ferruginous, euxinic and rare suboxic conditions. Although trace metal/TOC values imply extensive basin restriction, sustained trace metal enrichment and $\delta^{15}\text{N}_{\text{sed}}$ data indicate periodic access to open ocean inventories across a shallow-marine sill. Lastly, $\delta^{13}\text{C}_{\text{org}}$ values of between -35‰ and -40‰ allow at least partial correlation of the shales at Miaohe with Member IV of the Doushantuo Formation. This study provides evidence for fluctuating redox conditions in the lagoonal area of the Yangtze platform during the late Ediacaran. If these low-oxygen environments were

regionally characteristic, then the restriction of aerobic fauna to isolated environments can be inferred.

1. Introduction

The Neoproterozoic Era was characterised by intense environmental and biological change, and as such, marked a turning point in the development of the modern Earth system. Towards the end of this time (c. 575 Ma), came the emergence of the Ediacara Biota, representing the first large, structurally complex organisms (e.g. Narbonne & Gehling, 2003). This diversification of phyla has been hypothesised to be a result of increasing atmospheric and/or oceanic oxygen availability (e.g. Fike et al., 2006; Canfield et al., 2007). Termed the Neoproterozoic Oxygenation Event (NOE), the timing and extent of this environmental change has proved difficult to constrain (Shields-Zhou & Och, 2011). Moreover, recent studies (e.g. Canfield et al., 2008; Butterfield, 2009) indicate that oxygenation was more complex, with oceanic anoxia also common in the late Neoproterozoic, particularly along productive and restricted ocean margins (Sahoo et al., 2016; Tostevin et al., 2019). Alongside fluctuating oxygen levels, the Ediacaran was also characterised by events such as the Gaskiers glaciation and the global Shuram-Wonoka $\delta^{13}\text{C}$ negative anomaly (e.g. Condon et al., 2005), with the latter considered to represent oceanic oxygenation (Fike et al., 2006; Shields et al., 2019). To understand these events and the relationship between evolution and oxygenation during the late Neoproterozoic, it is important to focus on deposits containing both Ediacaran fauna and a lithology suited to geochemical analysis.

The ‘Miaohe Member’ shales at Miaohe (c. 560 to c. 551 Ma) in South China represent one lithological unit where combined geochemical and palaeontological study is possible. Because of this, several studies have been published examining the redox geochemistry and/or stratigraphy of these rocks (Li et al., 2015; An et al., 2015; Xiao et al., 2017). Contained within the shales at the Miaohe site is an assemblage comprising colonial prokaryotes, benthic multicellular algae and several putative metazoans (e.g. *Calyptrina* and *Jiuqunaoella*). These early organisms are preserved as carbonaceous compressions and collectively termed the ‘Miaohe Biota’ (Zhu & Chen, 1984; Chen & Xiao, 1992; Xiao et al., 2002). Importantly, this assemblage is believed to have been benthic (Xiao et al., 2002); redox data obtained from the Miaohe Member shales should therefore reflect changes in oxygenation at the potentially inhabitable sediment-water interface. Combining trace metal, Fe speciation and pyrite framboid data, Li et al. (2015) report that the Miaohe-Biota-associated black shales were deposited in a predominantly anoxic environment, with the remaining Miaohe Member shales deposited under euxinic (anoxic and sulfidic) conditions. Additional redox data are available from studies of the Doushantuo Formation Member IV (DST IV), a unit conventionally correlated with the ‘Miaohe Member’ (Zhu et al., 2013; Zhou et al., 2017; Xiao et al., 2017). Deposited between c. 635 Ma and c. 551 Ma, the Doushantuo Formation is of particular interest due to its widespread occurrence over much of South China and its variation in facies from deep marine to shallow marine shelf/lagoon (Zhu et al., 2003).

Geochemical proxies indicate a complicated redox environment during deposition of DST IV. Pyrite framboid analyses and Fe_{py}/Fe_{HR} and Fe_{HR}/Fe_T values from multiple Yangtze platform sites record dominantly euxinic conditions (Li et al., 2010; Li et al., 2015; Och et al., 2016; Sahoo et al., 2016). Enrichments of trace metals at multiple sites also suggest that DST IV deposition occurred under dominantly anoxic to euxinic bottom-water conditions (Li et al., 2010; Li et al., 2015; Och et al., 2016; Zhu et al., 2018). Despite this, several studies provide evidence for global oceanic oxygenation during deposition of DST IV (Scott et al., 2008; Kendall et al., 2015; Chen et al., 2015; Sahoo et al., 2016; Och et al., 2016; Shi et al., 2018; Ostrander et al., 2019). Observed Mo and V concentrations in DST IV indicate access to a large trace metal (oxyanion complex) inventory and globally extensive oxic seas (Scott et al., 2008; Sahoo et al., 2016; Och et al., 2016). Similarly, studies of $\delta^{34}S_{py}$, $\delta^{98}Mo$ and $\delta^{238}U$ data suggest that oceans were widely oxygenated at this time, and that oxyanion inventories remained high or even increased throughout the interval of DST IV deposition (McFadden et al., 2008; Kendall et al., 2015; Chen et al., 2015; Sahoo et al., 2016; Och et al., 2016; Wei et al., 2018; Ostrander et al., 2019; Shi et al., 2019). To explain the observed redox data, paleoenvironmental reconstructions typically include the presence of a metastable euxinic zone that controlled local redox conditions during deposition of DST IV (Li et al., 2010). A second major feature of the DST IV redox landscape is the occurrence of intra-shelf basins. In these shallow, lagoonal settings, positive $\delta^{34}S_{py}$ values, $\delta^{15}N$ data (Och et al., 2016) and infrequent Mo enrichment (Li et al., 2015) indicate a partially restricted environment, disconnected from global redox patterns (Och et al., 2016). To link this complex paleoenvironmental reconstruction with DST IV redox data from multiple sites across the Yangtze platform, a number of studies have examined the similarity of $\delta^{13}C$ data from different locations (Jiang et al., 2007; Li et al., 2010; Zhu et al., 2013; An et al., 2015; Zhou et al., 2017; Xiao et al., 2017; Li et al., 2017).

To understand water-column redox conditions contemporaneous to the deposition of the Miaohu Member facies, a multi-proxy approach is fundamental. In this study, Fe speciation, trace element (Mo, U, V and Cr) and $\delta^{14}N$ data are used to investigate water-column redox conditions and associated controlling factors during deposition of the Miaohu Member shales. An attempt is also made to integrate paleoredox proxy data with $\delta^{13}C$ data, thereby enabling the results of this study to be placed within a regional stratigraphic framework, while addressing recent uncertainties around the regional correlation of DST IV and the Miaohu Member (cf. Zhu et al., 2013; An et al., 2015; Zhou et al., 2017; Xiao et al., 2017). Additionally, while the potential impact of weathering on surface outcrop sample redox proxy data is well documented (e.g. Raiswell et al., 2018), we specifically address this issue by providing an example of secondarily-altered Fe speciation proxy data.

LOCATION OF FIGURE 1

2. Geological Setting and Study Sites

The Miaohe shales examined in this study have been described before in detail (e.g. Ding et al., 1996; Wang et al., 1998; Xiao et al., 2002). Paleogeographic reconstructions indicate that deposition of the Miaohe unit was along a carbonate-rich passive margin, in a shallow, shelf lagoon environment (Condon et al., 2005) (Fig. 1A). In this setting, redox variability would have been strongly controlled by the presence of a shelf margin complex that would have limited communication between the lagoon and deeper basin (Jiang et al., 2011). Conventionally, the Miaohe unit is considered to form the uppermost part of the Ediacaran Doushantuo Formation, which is today exposed in outcrop along the edge of the Huangling anticline in the Yangtze Gorges region of South China (Jiang et al., 2003). At this location, the Doushantuo Formation overlies the terminal Cryogenian Nantuo Formation, and is itself overlain by the upper Ediacaran Dengying Formation (Fig. 1B) (Xiao et al., 2017). Typically, the Doushantuo Formation in this area is considered to comprise a basal ~5 m thick dolostone (Member I); an overlying interbedded mudstone and argillaceous dolostone unit of ~70 m thickness (Member II); a ~40 m thick dolostone that passes upwards into an interbedded limestone and argillaceous dolostone; and a final ~20 m thick black shale unit (DST Member IV) (Jiang et al., 2006; Zhou & Xiao, 2007; McFadden et al., 2008; Jiang et al., 2011).

Although the Doushantuo Formation can be broadly traced around the circumference of the Huangling anticline, incomplete exposure has resulted in uncertainty over the stratigraphic placement of DST IV between localities (An et al., 2015; Zhou et al., 2017; Xiao et al., 2017). In particular, the relationship between DST IV described at Jiulongwan (Fig. 1B) and the ‘Miaohe Member’ examined in this study has proved difficult to reconcile. Due to subtle differences in the uppermost Doushantuo Formation between sections, Zhou et al. (2017) divided the Huangling study area into eastern, central and western zones (Fig. 1B). Notably, several locations in the ‘western zone’ (e.g. Miaohe, Qinglinkou, Jiuqunao and Sixi) show distinct variations when compared to the central and eastern zones; instead of the ~20 m thick black shale characteristic of Member IV at the Jiulongwan section, the rocks overlying Member III at these localities comprise two black shales separated by a dolostone unit (An et al., 2015; Xiao et al., 2017; Zhou et al., 2017). These three units have been termed the lower black shale (LBS), upper dolostone (UD) and Miaohe Member (M) (Zhou et al., 2017). Disruption is apparent at these localities in the western zone however, with regional-scale rotational sliding providing a likely mechanism for the observed repetition of the black shale and evident syn-sedimentary deformation within the upper dolostone (Zhu et al., 2013; Vernhet et al., 2007). Despite this, the original sequence of lithologies within Doushantuo Member IV remains controversial, with some studies partially correlating the Miaohe Member as described in the western zone (M) with Doushantuo Member IV (Zhou et al., 2017; Xiao et al., 2017), or partially with the younger Shibantan Member of the Dengying Formation (Fig. 1C) (An et al., 2015).

In this study, the ‘Miaohe Member’ shales from the Miaohe site are examined and compared with potentially correlative black shale units from the neighbouring Jiuqunao section and the Jiulongwan section further to the east (Fig. 1B). The succession at Miaohe comprises a series of finely laminated organic-rich black and siliceous shales, with occasional carbonate

concretions. Directly overlying the shales at Miaohé is an ~80 cm thick argillaceous dolostone that directly underlies, and potentially transitions into the Ediacaran Dengying Formation (Zhu et al., 2007; An et al., 2015; Xiao et al., 2017). In addition to anomalously low $\delta^{13}\text{C}_{\text{org}}$ and $\delta^{13}\text{C}_{\text{carb}}$ values (e.g. $\delta^{13}\text{C}_{\text{org}}$ values of between -22‰ and -40‰: Xiao et al., 2017), the black shales at the Miaohé site are notable for containing the ‘Miaohé Biota’, a collection of colonial prokaryotes and algal macrofossils preserved as carbonaceous compressions (Zhu and Chen, 1984; Chen and Xiao, 1992; Xiao et al., 2002). The Miaohé Biota occur over a 2 m interval, approximately 5-7 m from the base of the Miaohé shales at the Miaohé site (Xiao et al., 2002).

3. Geochemical redox proxies

3.a. Iron speciation

Iron geochemistry has been widely used as a method for discerning water-column redox conditions in both modern and ancient marine environments (e.g. Raiswell & Canfield, 1998; Raiswell et al., 2001; Poulton & Raiswell, 2002; Shen et al., 2002; 2003; Poulton et al., 2004). Sedimentary iron typically comprises carbonate-associated Fe (Fe_{carb}), ferric-oxides (Fe_{ox}), magnetite Fe (Fe_{mag}), pyrite Fe (Fe_{py}) and other poorly reactive or non-reactive iron-silicate minerals (Canfield, 1989; Raiswell et al., 1994; Raiswell and Canfield, 1996; 1998; Poulton et al., 2004). Poulton and Canfield (2005) developed a sequential extraction scheme to quantify operationally-defined Fe pools that broadly target these Fe phases, and this has been widely used to distinguish anoxic-ferruginous, euxinic and oxic water-bodies (see Poulton & Canfield, 2011; Poulton 2021). In this scheme, Fe_{carb} , Fe_{ox} , Fe_{mag} and Fe_{py} constitute the highly reactive iron pool (Fe_{HR}), and Fe_{HR}/Fe_T and Fe_{py}/Fe_{HR} ratios are used together to define the redox state of the water-column.

Observations from both modern and Phanerozoic sediments indicate that an Fe_{HR}/Fe_T threshold of 0.38 generally marks the upper limit for deposition of sediments in an oxic water-column, with values of >0.38 indicative of anoxia (Raiswell & Canfield, 1998; Poulton & Canfield, 2011). Sediments deposited rapidly in an anoxic environment have been documented to record lower Fe_{HR}/Fe_T ratios, however (Raiswell & Canfield, 1998), and caution should be applied when interpreting ratios between 0.22 and 0.38 (Poulton & Canfield, 2011; Raiswell et al., 2018; Poulton, 2021). As defined empirically, an Fe_{py}/Fe_{HR} value of <0.6 – for samples with $Fe_{HR}/Fe_T >0.38$ – likely indicates ferruginous conditions (Benkovitz et al., 2020; Poulton, 2021), whereas a value of >0.8 suggests euxinia (Poulton et al., 2004; Canfield et al., 2008). Fe_{py}/Fe_{HR} values between 0.6 and 0.8 should be interpreted with caution (Poulton and Canfield, 2011; Poulton, 2021). Generally, Fe_{HR}/Fe_T and Fe_{py}/Fe_{HR} proxies should both be applied with consideration for the depositional environment (including rate of deposition, sediment composition, fluctuating redox conditions and biological/physical reworking), Fe_T content, post-depositional alteration and surface weathering of pyrite (Clarkson et al., 2014; Raiswell et al., 2018).

3.b. Redox-sensitive trace metals

The enrichment of redox-sensitive trace metals in organic-rich shales can also be used to decipher paleoredox conditions. Due to changes in solubility, the burial fluxes of Mo, V, U and Cr are several orders of magnitude larger in reducing environments than in an oxidising environment (Emerson & Husted, 1991). In a euxinic setting, amplification of Mn/Fe redox cycling and the availability of organic carbon substrates is increased, thereby influencing patterns of trace metal enrichment (Morse & Luther, 1999; Algeo & Maynard, 2004).

In seawater, molybdenum occurs as the molybdate oxyanion complex, MoO_4^{2-} (Broecker & Peng, 1982). Given reducing conditions, molybdate is readily sequestered by Mn-oxyhydroxides at the sediment-water interface and released to pore waters (Bertine &

Turekian, 1973; Calvert & Pedersen, 1993; Crusius et al., 1996; Erickson & Helz, 2000; Zheng et al., 2000; Goldberg et al., 2012). In the presence of free H₂S, molybdate present in sediment pore water is able to react to form particle-reactive thiomolybdates (MoO_xS_{4-x}) (Helz et al., 1996), which are easily scavenged by sulfur-rich organic molecules, metal-rich compounds (Helz et al., 1996, 2011; Tribovillard et al., 2004) and FeS (Vorlicek et al., 2004; Poulson Brucker et al., 2012). Although moderately enriched in sediments deposited in non-sulfidic anoxic conditions, Mo is more strongly enriched in sediments deposited in a euxinic environment (e.g. Tribovillard et al., 2006).

In an oxic water-mass, Vanadium occurs as vanadate oxyanions (HVO₄²⁻ and H₂VO₄⁻), which are readily adsorbed onto both Mn- and Fe-oxyhydroxides (Calvert & Piper, 1984; Wehrli & Stumm, 1989). In anoxic conditions, V(V) is readily reduced to V(IV), forming vanadyl (VO²⁺) and hydroxyl (VO(OH)₃⁻) species, in addition to insoluble hydroxides (VO(OH)₂). The resulting ions can then be scavenged via organometallic ligand formation or surface adsorption (Emerson & Husted, 1991; Morford & Emerson, 1999). Given a more strongly reducing euxinic environment, V(V) is further reduced to V(III), which can be taken up by geoporphyrins, or precipitated as solid V₂O₃ oxides or V(OH)₃ hydroxides (Breit & Wanty, 1991; Wanty & Goldhaber, 1992). Unlike Mo, V is readily sequestered and enriched in sediments deposited in a reducing but non-sulfidic water-column (e.g. Algeo & Maynard, 2004; Tribovillard et al., 2006).

Uranium is mainly present in seawater as carbonate-bound uranyl ions, UO₂(CO₃)₃⁴⁻ (Anderson et al., 1989). In an anoxic environment, the reduction of U(VI) to U(IV) forms UO²⁺ uranyl ions or less-soluble uranous fluoride compounds and occurs independently to Fe and Mn cycling. Because of this, U enrichment primarily takes place within the sediment (Anderson et al., 1989; Algeo & Maynard, 2004; McManus et al., 2005). At this location, U accumulates due to adsorption by humic acid ligand complexes or the precipitation of uraninite (UO₂), U₃O₇ or U₃O₈ (e.g. Klinkhammer & Palmer, 1991; Crusius et al., 1996; McManus et al., 2005). The presence of free H₂S and active sulfate reduction is thought to accelerate the latter process (Langmuir, 1978; Klinkhammer & Palmer, 1991). Typically, U is enriched in non-sulfidic anoxic facies and strongly enriched in euxinic facies, although vulnerable to remobilisation and secondary depletion (e.g. Algeo & Maynard, 2004; Tribovillard et al., 2006).

In oxic seawater, Cr mainly occurs as the chromate oxyanion, CrO₄²⁻ (Cranston & Murray, 1978). In an anoxic setting, Cr(IV) is readily reduced to Cr(III), subsequently forming hydroxyl and aquahydroxyl cations (e.g. Cr(OH)₂⁺). These cations are able to react to form insoluble Cr(OH)₃ and Cr₂O₃, or complex with humic/fulvic acids to enable adsorption by Fe- and Mn-oxyhydroxides, thereby enabling transport of Cr to the sediment (Elderfield, 1970; Emerson et al., 1979; Breit & Wanty, 1991; Algeo & Maynard, 2004). In sulfidic conditions, structural and electronic incompatibilities limit uptake of Cr (III) by Fe-sulfides (Huerta-Diaz & Morse, 1992; Morse & Luther, 1999). As a result, Cr is typically enriched in anoxic sediments, with little change to the relative degree of anoxic enrichment under euxinic conditions (e.g. Algeo & Maynard, 2004).

The behaviour demonstrated by each of the redox-sensitive trace elements, Mo, U, V and Cr creates relative patterns of sedimentary enrichment. Firstly, strong Cr, V and/or U enrichment without strong Mo enrichment indicates anoxic but not euxinic conditions, while strong Mo, U or V enrichment without strong Cr enrichment indicates euxinia (Algeo & Maynard, 2004; Tribovillard et al., 2006). In a suboxic ($O_2 < 5 \mu M$) water-column, Mo, U, V and Cr solubilities are all increased and sedimentary enrichment is therefore low (Algeo & Maynard, 2004). Commonly, trace metal enrichment/depletion is assessed by normalisation to a reference shale (Wedepohl, 1971, 1991; McLennan, 2001; Tribovillard et al., 2006; Algeo & Tribovillard, 2009). In anoxic basins, the uptake of Mo, U and V is also closely linked to the availability of TOC. This is because reduced metal species such as thiomolybdate and vanadyl ions are bound by organic particles (Lyons et al., 2009). Because of this, trace metal/TOC ratios can be used as paleogeographic proxies for understanding the extent of basin restriction and deep-water renewal (Algeo & Lyons, 2006; Algeo & Rowe, 2012).

3.c. Nitrogen Isotopes

The isotopic signature ($\delta^{15}N_{sed}$) of nitrogen in marine sediments is linked to multiple biogeochemical processes, including nitrification, denitrification, nitrogen fixation and anammox. During denitrification, NO_3^- is reduced to N_2 or N_2O , and the seawater nitrate reservoir is enriched in ^{15}N relative to atmospheric nitrogen ($\delta^{15}N = 0\%$) due to isotopic fractionation (Sigman et al., 2009; Kikumoto et al., 2014). Conversely, diazotrophic N_2 fixation results in slightly negative $\delta^{15}N_{sed}$ values (e.g. Zhang et al., 2014; Ader et al., 2014). Due to the near-complete ventilation of modern oceans, present-day $\delta^{15}N_{sed}$ values have a mode of +5-6‰, with an overall range of between +1‰ and +15‰ (Tesdal et al., 2013; Ader et al., 2014). This is due to nitrate limitation, whereby denitrification and/or assimilation exceed oceanic nitrate input/recycling (e.g. Kikumoto et al., 2014).

Because of the link between oxygenation and marine productivity, $\delta^{15}N_{sed}$ values can be tentatively used as paleoredox proxies (e.g. Sigman et al., 2009). In a redox-stratified ocean, the oxic-anoxic interface is elevated in the water-column. In deeper, anoxic waters, the nitrogen generated by biological processes will be in the form of ammonium (NH_4^+), while in oxygenated surface waters organic nitrogen will be converted to NO_3^- . In this scenario, $\delta^{15}N_{sed}$ values strongly relate to both the depth of the redox transition zone and mixing (upwelling) between the deep ammonium pool and the shallow nitrate-rich pool. Although difficult to standardise, typical $\delta^{15}N_{sed}$ values from primarily anoxic settings tend towards 0‰ (Quan & Falkowski, 2009; Ader et al., 2014). In a euxinic water-column, N_2 fixation is favoured and occurs with a fractionation of between 0 to -2‰, further reducing $\delta^{15}N_{sed}$ values (Cremonese et al., 2013). Because of the variability associated with $\delta^{15}N_{sed}$ in modern marine settings, $\delta^{15}N_{sed}$ should only be used for local paleoredox reconstructions in conjunction with other established proxies (Quan et al., 2008).

4. Materials and methods

The 20 surface outcrop samples used in this study were collected from the 'Miaohe Member' black shales at Miaohe (Fig. 1B). Small portions were obtained from clean surface sections and powdered for geochemical analysis.

4.a. Iron speciation

Several operationally-defined Fe pools were measured during iron speciation analysis (Poulton & Canfield, 2005). These are carbonate-associated Fe (Fe_{carb}), ferric-oxides (Fe_{ox}), magnetite Fe (Fe_{mag}) and pyrite Fe (Fe_{py}). Total Fe was also measured (Fe_T).

Fe_{py} was measured using an adaptation of the method outlined by Canfield et al. (1986). Initially, between 2-4 g of gravimetrically measured powdered sample was placed in a digestion flask, to which 8 ml of concentrated HCl was added. After heating under a constant flow of N_2 to determine whether acid volatile sulfide (AVS) was present (no AVS was detected), 16 ml of acidified $CrCl_2$ was added to the solution and heated to boiling for 2 hours, during which time any liberated H_2S was collected in a $AgNO_3$ trap as Ag_2S . The concentration of Fe_{py} was then determined gravimetrically.

The remaining Fe pools (Fe_{ox} , Fe_{mag} and Fe_{carb}) were measured following the sequential extraction technique of Poulton and Canfield (2005). Between 50-100 mg of powdered sample was placed in a centrifuge tube. To each of the samples, 10 ml of 1 M sodium acetate (adjusted to a pH of 4.5 with acetic acid) was added and constantly agitated for 48 hours at a temperature of 50°C. After centrifugation and removal of the supernatant, 10 ml of 0.28 M sodium dithionite (adjusted to a pH of 4.8 with 0.2 M acetic acid and 0.3 M tri-sodium citrate) was added and shaken for 2 hours at ambient temperature. For the final step, 10 ml of 0.2 M ammonium oxalate (buffered with 0.17 M oxalic acid) was added and shaken for 6 hours at ambient temperature.

Fe_T was measured via a multi-acid digestion. Initially, 100 mg of each sample was ashed at 450°C for 8 hours. Following this, 5 ml of concentrated HNO_3 , 2 ml of HF and 2-3 drops of $HClO_4$ were added. The solutions were then heated and left to dry, after which boric acid was added and evaporated to dryness. The samples were then re-dissolved in concentrated HNO_3 .

Dissolved iron concentrations were measured using Atomic Absorption Spectroscopy (AAS). Replicate analyses of PACS-2, an international sediment standard, gave a RSD of <5% for all sequential extraction stages, and an Fe_T accuracy of >98%. Iron speciation analyses were performed in the Cohen Geochemistry Laboratory, University of Leeds.

4.b. Redox-sensitive trace metals

The trace metal (Mo, U, V and Cr) content of each sample was measured via multi-acid digestion. Firstly, 3 ml of HF and 2 ml HNO_3 were added to 60 mg of powdered sample and the mixture heated at 200°C for 16 hours. The resulting solution was left to cool and evaporate to dryness. A further 2 ml of HF, 1 ml of HNO_3 and 2 ml of $HClO_4$ were added and the solution was again heated at 200°C for 16 hours. This solution was left to cool and

evaporate before 1 ml of HNO₃ and 1 ml of HClO₄ were added. Following a final phase of cooling and evaporation to dryness, 1 ml of HNO₃ was added. 1 ml aliquots for each sample were then analysed using Inductively Coupled Plasma Mass Spectrometry (ICPMS) at the instrument laboratory of the London Geochemistry and Isotope Centre (LOGIC), University College London.

4.c. Stable isotopes

Analyses were performed at the Bloomsbury Environmental Isotope Laboratories (BEIF) of University College London, using a Thermo Finnigan Elemental Analyzer Mass Spectrometer (continuous flow). Rock samples were first washed, cut into small chips and ground after removing altered and recrystallized fragments. An amount of rock powder between 10 mg and 200 mg was used for nitrogen isotope analyses depending on the expected nitrogen concentration. The error associated with $\delta^{15}\text{N}$ and $\delta^{13}\text{C}_{\text{org}}$ is $\pm 0.50\%$. Some samples needed to be analysed repeatedly, in order to ensure a meaningful nitrogen isotope signal, although here we publish only the highest-fidelity values based on the signal background and peak intensity. $\delta^{15}\text{N}$ values were calibrated during each session using the minor internal standard drift experienced by the EA.

4.d. Total organic carbon (TOC)

TOC values were determined after first adding 10 ml of 10% HCl to 1000 mg of sample. Samples were then centrifuged and the supernatant discarded, before being rinsed and dried at 50°C overnight. Carbon was then measured using a Leco C/S analyser (Leco Corporation, St Joseph, MI, USA) at the London Geochemistry and Isotope Centre (LOGIC), University College London.

4.e. Redox-sensitive trace metal enrichment factors

Trace metal concentrations are commonly normalised to the concentrations of detrital elements such as Al, Ti and Sc and presented as ‘enrichment factors’ (e.g. Tribovillard et al., 2006; Algeo & Tribovillard, 2009). In this study, Mo, V, U and Cr enrichment factors were calculated using the equation: $EF_x = ([X]/\text{Ti}_{\text{sample}})/([X]/\text{Ti}_{\text{upper continental crust}})$. Average upper continental crust trace metal concentrations for normalisation were obtained from McLennan (2001).

5. Results

5.a. Samples

Although several of the samples associated with the Miaohé Biota-bearing strata are dark shales, the majority of samples powdered for geochemical analysis were evidently silicified. Relatively immobile metals Ti, Sc, Th and REE all covary linearly (see Supplementary Material) but are significantly depleted in all samples relative to upper continental crust (McLennan, 2001), indicating that Fe concentrations have been diluted by silica and/or other non-silicate minerals to varying extents. Because of this silicification, a minority of the samples analysed record Fe_T values below the 0.5 wt. % threshold conventionally considered appropriate for Fe speciation analyses (Clarkson et al., 2014; Raiswell et al., 2018). Similar Fe_T values are recorded in equivalent Miaohé Member samples obtained by Li et al. (2015), and for the subset of samples from both studies that contain <0.5 wt. % Fe_T , Fe speciation analyses must be considered to be potentially ambiguous.

The hand specimens used in this study showed visible evidence of oxidative weathering, particularly along previously exposed surfaces (see Supplementary Material; Fig. 2). As previously discussed, Fe speciation proxies should only be applied with consideration for the environment of deposition, potential post-depositional alteration and the impact of weathering (Clarkson et al., 2014; Raiswell et al., 2018). Equivalent samples obtained by Li et al. (2015) were excavated at depth, while those obtained for this study are surface outcrop samples; a comparison of the two studies therefore provides an opportunity to quantitatively assess the impact of clear visible surface weathering on Fe speciation data. Unlike the weathered samples evaluated in this study, and despite evidence of increased Fe_{ox} in some samples (Fig. 3), Li et al. (2015) argue that the presence of microscopic pyrite framboids means any significant impact due to oxidative weathering is unlikely for their excavated samples. These differences are demonstrated by the mean Fe_{py}/Fe_{HR} values of 0.04 and 0.46 recorded in this study and by Li et al. (2015), respectively.

LOCATION OF FIGURE 2

5.b. Iron speciation

Although a study by Ahm et al. (2017) found a difference of up to 30% for Fe_{HR}/Fe_T data between outcrop and core samples from the Vinini Formation in Nevada, USA, it is likely that the Fe_{HR}/Fe_T proxy is mostly unaffected by modern oxidative weathering. Previously, a study of 231 carbonate samples (Sperling et al., 2013) found no statistical correlation between Fe_{py}/Fe_{HR} and Fe_{HR}/Fe_T data despite pyrite weathering, thereby implying that the Fe_{py} fraction is transformed into immobile iron (oxyhydr)oxides that are preserved in the vicinity of the original pyrite. This is consistent with the behaviour of Fe during chemical weathering (Poulton and Raiswell, 2002). Because of this, the Fe_{HR}/Fe_T proxy can be used despite evidence of secondary oxidative weathering. The Miaohé section shales record Fe_{HR}/Fe_T values of between 0.46 and 0.9 (Table 1; Fig. 5), suggesting that deposition occurred in a sustained anoxic setting. It is important to note that although several of the samples used in this study record Fe_T concentrations of <0.5 wt. %, Fe_{HR}/Fe_T ratios from all

samples analysed consistently record anoxia. These values are also similar to the Fe_{HR}/Fe_T ratios obtained by Li et al. (2015).

Fe_{py}/Fe_{HR} values ($0.00 \leq Fe_{py}/Fe_{HR} \leq 0.41$) appear to indicate anoxic-ferruginous conditions. However, as discussed in Section 5.a., evidence for pyrite weathering and Fe_{ox} enrichment (e.g. samples M0.5, M14 and M10; Table 1; Fig. 3) together imply that primary Fe_{py}/Fe_{HR} may have been diminished due to secondary alteration. Similar Fe_{py}/Fe_{HR} data from Li et al. (2015) ($0.07 < Fe_{py}/Fe_{HR} < 0.92$) are likely more representative of water-column redox state, particularly in the uppermost, non-fossiliferous section, where Fe_{py}/Fe_{HR} ratios suggest euxinia ($0.74 \leq Fe_{py}/Fe_{HR} \leq 0.92$, with one exception at 15.4 m).

LOCATION OF FIGURE 3

5.c. Redox-sensitive trace metals

Although most samples studied record Mo, U, V and Cr enrichment relative to average shale values (McLennan, 2001), four discrete ‘zones’ of trace metal enrichment can be identified (Fig. 5). The first zone occurs between 2 – 3 m stratigraphic height and records moderate trace metal enrichment (e.g. Mo EFs of 4.29 – 5.46, U EFs of 2.96 – 4.92, Cr EFs of 2.35 – 3.68). For this interval, Mo EFs are increased relative to Cr. Mo/TOC, U/TOC and V/TOC values are low, at 0.91, 1.16 and 21.71 respectively. From 3 – 12 m, trace metal enrichment is generally reduced and Mo is depleted relative to Cr (Mo EFs of 0.89 – 3.26, Cr EFs of 1.73 – 3.23). Although increased, trace metal/TOC values remain low over this interval (Mo/TOC of 0.35 – 1.40, U/TOC of 0.90 – 3.46, V/TOC of 24.04 – 149.22). A third zone occurs between 12 – 21 m stratigraphic height and is characterised by increased trace metal enrichment (Mo EFs of 2.32 – 11.09, V EFs of 1.77 – 4.62, U EFs of 2.64 – 9.97, Cr EFs of 2.43 – 5.76). Mo EFs are greater than Cr EFs, and low trace metal/TOC values similar to the first interval are also recorded (Mo/TOC of 0.49 – 1.01, U/TOC of 1.02 – 2.08, V/TOC of 18.85 – 43.02). Lastly, a zone of reduced trace metal enrichment is recorded between 21 – 26.4 m (Mo EFs of 2.91 – 5.06, U EFs of 2.30 – 3.64, Cr EFs of 1.83-2.68). Patterns of trace metal enrichment are not observed and there is no clear relationship between Cr and Mo. V does not show enrichment, with recorded V EFs of between 0.84 – 1.26 typical of average shale values. Although initially low, Mo/TOC, U/TOC and V/TOC values rapidly increase with increasing stratigraphic height (e.g. Mo/TOC values of 0.47, 1.11 and 9.20 at 22.9 m, 24.9 m and 26.4 m, respectively).

As discussed previously, the samples used in Li et al. (2015) are less weathered than those used in this study (Fig. 3), thereby providing an opportunity to investigate the potential effects of weathering on the distribution of redox-sensitive trace metals. The mean concentrations of Mo, V, and Cr in our weathered samples are lower (Supplementary Material) and statistically different (t-test, p-values <0.05) to those from Li et al. (2015). The mean enrichment factors are statistically different for Cr and V (t-test, p-values <0.05) but statistically indistinguishable for Mo (t-test, p-values >0.05) (Supplementary Material). This suggests that the recorded enrichments of redox-sensitive trace metals may have been altered by weathering to some extent. Despite the discrepancy in enrichment factor values, the

stratigraphic trends are broadly consistent and the impact on paleoredox interpretation is limited.

5.d. Nitrogen isotopes

Sedimentary TN values for the Miaohe section samples range from 0.006 wt. % to 0.057 wt. % (mean of 0.024 wt. %). $\delta^{15}\text{N}$ data are generally consistent, ranging from 3.85 ‰ at 5 m stratigraphic height, to 1.64 ‰ at 18.2 m stratigraphic height (Table 1; Fig. 5). Generally, $\delta^{15}\text{N}$ data shows a steady decrease with increasing stratigraphic height upwards through the Miaohe section.

Although it is possible that clay-bound nitrogen may have influenced nitrogen isotope values, the strong positive covariation between TN and TOC ($R^2=0.64$; Supplementary Material) together with a near-zero intercept for Miaohe Member shales, suggests that any contribution from allochthonous clay-bound N is limited. In addition, thermal nitrogen volatilization preferentially removes ^{14}N during thermal maturation. There is no obvious covariation between $\delta^{15}\text{N}$ and TN values for the Miaohe Member shales (Supplementary Material), indicating limited impact on $\delta^{15}\text{N}$ values.

5.e. Carbon isotopes

Sedimentary TOC values for the Miaohe section samples range from 0.10 wt. % to 2.69 wt. % (mean of 1.19 wt. %) (Table 1). With the exception of a calcareous sample at 26.4 m stratigraphic height, $\delta^{13}\text{C}_{\text{org}}$ values range from -36.7‰ to -38.3‰ (Table 1; Fig. 4) and therefore occur within the DST IV domain (McFadden et al., 2008; Li et al., 2010; Wang et al., 2014; Xiao et al., 2017). Generally, a subtle $\sim 3\%$ increase in $\delta^{13}\text{C}_{\text{org}}$ values with increasing stratigraphic height is observed. At Jiuqunao, TOC values for the upper black shale range from 0.55 wt. % to 5.63 wt. % (mean of 2.80 wt. %). Similar to at Miaohe, $\delta^{13}\text{C}_{\text{org}}$ values at Jiuqunao are between -37.3‰ and -38.1‰ and therefore consistently occur within the DST IV domain (Fig. 4). A slight increase in $\delta^{13}\text{C}_{\text{org}}$ values with increasing stratigraphic height is also observed. The $\delta^{13}\text{C}_{\text{org}}$ values at Jiulongwan range from -33.9‰ to -38.4‰ (Fig. 4). A trend of increasing $\delta^{13}\text{C}_{\text{org}}$ values upwards is observed, with the lower 10 samples recording values of less than -35‰, and the highest values occurring close to the boundary with the overlying Dengying Formation.

In general, thermal maturation during catagenesis and/or metagenesis would lead to preferential removal of ^{12}C and loss of organic matter, thereby creating a diagnostic negative correlation between TOC and $\delta^{13}\text{C}_{\text{org}}$ values. In the Miaohe section, only a very weak covariation between TOC and $\delta^{13}\text{C}_{\text{org}}$ values is observed (Supplementary Material). This suggests that the organic carbon isotopes have not been significantly influenced by thermal maturation.

6. Discussion

6.a. Carbon isotopes: chemostratigraphy and regional placement

LOCATION OF FIGURE 4

Constraining the link between the Miaohu Biota and $\delta^{13}\text{C}$ data at Miaohu, relative to $\delta^{13}\text{C}$ data at adjacent sites, is necessary to ensure that a stratigraphic framework is developed for the Doushantuo Formation that allows broader Ediacaran correlation. Recorded $\delta^{13}\text{C}_{\text{org}}$ data for the Shibantan Member and DST IV at Jiulongwan are discrete; typically, Shibantan Member $\delta^{13}\text{C}_{\text{org}}$ values are between -25‰ to -30‰ (Wang et al., 2014), while DST IV $\delta^{13}\text{C}_{\text{org}}$ values are constrained to between -35‰ to -40‰ (McFadden et al., 2008; Li et al., 2010; Wang et al., 2014; Xiao et al., 2017). With the exception of a single calcareous sample at the Doushantuo-Dengying boundary, the $\delta^{13}\text{C}_{\text{org}}$ data obtained from the Miaohu Member at Miaohu in this study are remarkably similar to $\delta^{13}\text{C}_{\text{org}}$ data (this study; McFadden et al., 2008; Li et al., 2010; Wang et al., 2014) from DST IV at Jiulongwan (Fig. 4). It is therefore simple to infer at least partial correlation between the Miaohu Member and DST IV, and reject the inferred partial correlation with the younger Shibantan Member as proposed by An et al. (2015). In Xiao et al. (2017), the main objection to this correlation (termed the ‘Z’ correlation therein) was that several samples from the Miaohu Member at Miaohu record $\delta^{13}\text{C}_{\text{org}}$ values within the ‘Shibantan Domain’. Interestingly, $\delta^{13}\text{C}_{\text{org}}$ values from the same section in this study are significantly less variable, conforming to recorded values from DST IV at Jiulongwan (McFadden et al., 2008; Li et al., 2010; Wang et al., 2014; this study) and Jiuqunao (this study).

Patterns of $\delta^{13}\text{C}_{\text{org}}$ data also provide support for correlation of the Miaohu Member with DST IV (Fig. 4). At Jiulongwan, Jiuqunao, Miaohu and the drillcore site described by Kikumoto et al. (2014), $\delta^{13}\text{C}_{\text{org}}$ data for the Miaohu Member (Miaohu, Jiuqunao) and DST IV (Jiulongwan, drillcore) behave similarly, with $\delta^{13}\text{C}_{\text{org}}$ values for all sites and from all datasets increasing. Below the contact with the overlying Dengying Formation, several datasets also show an abrupt increase in $\delta^{13}\text{C}_{\text{org}}$ values (Jiuqunao: this study; Li et al., 2010; Wang et al., 2014 and Kikumoto et al., 2014). Although the increase at Miaohu is less pronounced, the uppermost sample from this study records a $\delta^{13}\text{C}_{\text{org}}$ value of -34.82‰, a significant increase from -36.72‰ recorded 1.5 m deeper in the section. Interestingly, this sample is calcareous, and although originally interpreted as part of the basal Hamajing Member, may have been collected from a minor argillaceous carbonate bed, similar to those observed at Jiulongwan (An et al., 2015; Xiao et al., 2017) and Jiuqunao (Condon et al., 2005; Zhu et al., 2007; Lu et al., 2013; An et al., 2015; Xiao et al., 2017). Although considered in this study to form part of the upper Doushantuo Formation, placement of this >1 m thick carbonate unit has proved difficult; at Jiuqunao, it has been variously regarded as part of the basal Dengying Formation (Lu et al., 2013) or upper Doushantuo Formation (Condon et al., 2005; Zhu et al., 2007; An et al., 2015; Xiao et al., 2017). In addition to uncertainty over placement of this minor carbonate unit, it should be noted that the Dengying-Doushantuo contact is transitional, with variable expression depending on locality. It is unlikely therefore that the Dengying-Doushantuo contact has been consistently interpreted between sites. At Jiuqunao, an ash bed found

underlying the minor argillaceous carbonate unit is used to date the uppermost Miaohe Member (550.55 ± 0.75 Ma, Condon et al., 2005; 551.09 ± 1.02 Ma, Schmitz, 2012) and the placement of the minor carbonate bed therefore has implications for constraining the timing of deposition of the Miaohe Member.

At Jiulongwan, Jiuqunao and Miaohe, $\delta^{13}\text{C}_{\text{carb}}$ data further support correlation of the Miaohe Member with DST IV. For each site, multiple datasets record the same trend: an increase from negative $\delta^{13}\text{C}_{\text{carb}}$ values at the Dengying-Doushantuo contact, to positive values further up the section (Jiang et al., 2007; Wang et al., 2014; An et al., 2015; Zhou et al., 2017; Xiao et al., 2017) (Fig. 4). This similarity between not only $\delta^{13}\text{C}_{\text{org}}$ data, but $\delta^{13}\text{C}_{\text{carb}}$ data for Miaohe, Jiulongwan, Jiuqunao and the drillcore site is unlikely to be coincidental, and a potential third correlation – that the Miaohe Member cannot be correlated with either the Shibantan Member or DST IV – as tentatively discussed in Xiao et al. (2017), can be rejected.

The DST IV $\delta^{13}\text{C}_{\text{org}}$ and $\delta^{13}\text{C}_{\text{carb}}$ data from Baiguoyuan, a site located along the northern flank of the Huangling anticline (Qian et al., 1995; Zhuang et al., 1999; Wallis, 2006; Zhu et al., 2013; Och et al., 2016), provides further support for correlation of DST IV with the Miaohe Member at Miaohe. For this section, the same upward recovery of $\delta^{13}\text{C}_{\text{carb}}$ data (from -7.42% to $+4.86\%$) is recorded across the Dengying-Doushantuo contact, while $\delta^{13}\text{C}_{\text{org}}$ data for DST IV remains within the ‘DST IV domain’ (see Xiao et al., 2017) and shows a consistency similar to $\delta^{13}\text{C}_{\text{org}}$ data from DST IV at Jiulongwan (this study; McFadden et al., 2008; Li et al., 2010; Wang et al., 2014) and the Miaohe Member at Jiuqunao and Miaohe (this study).

Although $\delta^{13}\text{C}$ data provide evidence for correlation of the Miaohe Member at Jiuqunao and Miaohe with DST IV, placement of the LBS unit is less clear. An et al. (2015) correlate the LBS with DST IV, while Zhou et al. (2017) and Xiao et al. (2017) consider the sum of the LBS, intermediate dolostone and Miaohe Member to correlate with DST IV. Zhou et al. (2017) suggest that in the latter scenario, an eastward facies change would result in the disappearance of the intermediate dolostone in the Central Zone (Fig. 1B). Considering that basinal-scale rotational sliding occurred during deposition of the overlying lower Dengying/Liuchapo Formation (e.g. Vernhet et al., 2007; Zhu et al., 2013), and the recognition that such a slide is present at Miaohe (Zhu et al., 2013), we consider it more likely that the LBS, when present, represents a portion of DST IV that has acted as a slip surface, carrying deformed dolostones of the Hamajing Member (the intermediate dolostone with positive $\delta^{13}\text{C}_{\text{carb}}$ values). This interpretation appears the most parsimonious explanation for the lack of such units, or related isotopic complexity at the relatively undisturbed Jiulongwan section in the east.

6.b. Paleoredox proxies

LOCATION OF FIGURE 5

Several studies indicate that the oceanic redox environment of southern China during the Ediacaran was spatially complex (e.g. Li et al., 2010; Li et al., 2015; Och et al., 2016; Sahoo et al., 2016; Zhu et al., 2018). Previous Fe speciation, trace metal and pyrite framboid analyses from the Miaohu Member at Miaohu indicate that deposition of the lower, Miaohu Biota-associated shales was in a suboxic to anoxic but non-sulphidic environment, while the uppermost shales were deposited under euxinic conditions (Li et al., 2015). At the adjacent Jiulongwan and Jiuqunao sites, Fe speciation, trace metal and pyrite framboid data provide evidence for deposition in dominantly euxinic conditions (Li et al., 2010; Li et al., 2015). New Fe speciation, trace metal and $\delta^{15}\text{N}$ data are discussed below, providing additional redox information for the period of deposition of the Miaohu Member at Miaohu.

6.b.1. Iron speciation & redox-sensitive trace metals

In this study, $\text{Fe}_{\text{HR}}/\text{Fe}_{\text{T}}$ values are all >0.46 and therefore suggest persistent anoxia during deposition of the Miaohu Member (Fig. 5). Although Li et al. (2015) mainly record $\text{Fe}_{\text{HR}}/\text{Fe}_{\text{T}}$ values greater than the anoxic threshold (0.38) for the same section, several values between 4.9 m and 6.9 m occur within the ‘possibly anoxic’ and ‘oxic’ domains, roughly the same stratigraphic height as the preserved Miaohu Biota (Fig. 5). It should be noted, however, that Li et al. (2015) record a greater number of data points over the fossiliferous section, and that the $\text{Fe}_{\text{HR}}/\text{Fe}_{\text{T}}$ data with the lowest values from this study occur over roughly the same interval.

Although most of the Miaohu Member at Miaohu was likely deposited in an anoxic water-column, distinguishing euxinic and anoxic-ferruginous conditions is more complex. The $\text{Fe}_{\text{py}}/\text{Fe}_{\text{HR}}$ ratios obtained in this study ($0.00 \leq \text{Fe}_{\text{py}}/\text{Fe}_{\text{HR}} \leq 0.41$) cannot be relied upon due to secondary pyrite weathering (see Section 5.a.; Figs. 2, 3 & 6). $\text{Fe}_{\text{py}}/\text{Fe}_{\text{HR}}$ data obtained from rocks of the same site and stratigraphic setting by Li et al. (2015) are consistently higher ($0.07 \leq \text{Fe}_{\text{py}}/\text{Fe}_{\text{HR}} \leq 0.92$), and in the uppermost ~ 10 m, indicative of euxinia (Fig. 5). In this current study, patterns of trace metal enrichment also support at least periodic euxinia, particularly in the uppermost Miaohu Member. For clarity, five discrete zones can be discerned using trace metals (Fig. 5): (1) euxinia from 2-3 m as indicated by moderate overall trace metal enrichment and an increased enrichment of Mo relative to Cr; (2) anoxic, non-sulphidic conditions between 3-6.5 m and 7.5-12 m, as indicated by an overall decrease in trace metal enrichment and the increased enrichment of Cr relative to Mo; (3) persistent euxinia between 12-21 m as indicated by a relatively rapid increase in trace metal enrichment, and an increased enrichment of Mo relative to Cr; (4) an anoxic, but not necessarily sulphidic environment, as indicated by decreasing trace metal concentrations and similar enrichments of Mo and Cr from 21-26.4 m, and (5) an anoxic to suboxic setting during deposition of the shales from 7-8 m, whereby enrichments in U and V are minor and Mo is depleted (Fig. 3). Trace metal data for the same section from Li et al. (2015) are indicative of suboxic to anoxic, but non-sulphidic conditions; notably, Mo concentrations are <3 ppm and therefore close to crustal values. The $\text{Fe}_{\text{py}}/\text{Fe}_{\text{HR}}$ ratios from Li et al. (2015) for the lower Miaohu-Biota associated shales mostly fall within the ferruginous domain (Figs. 5, 6), although it is important to note that the proportion of Fe_{ox} found in some of these samples (e.g. MH-5 & MH-9, Li et al., 2015) could indicate secondary pyrite weathering (Fig. 3). Li et al.

(2015) suggest that any impact of weathering on their samples was limited, however, it remains possible that the ferruginous signal recorded by the lowermost shales is inaccurate.

LOCATION OF FIGURE 6

6.b.2. Nitrogen Isotopes

Nitrogen isotope ($\delta^{15}\text{N}_{\text{sed}}$) values from Miaohe Member samples are generally stable between 1.5‰ to 4‰, with the highest $\delta^{15}\text{N}_{\text{sed}}$ values found in the lower half of the section (Fig. 5). Together with iron speciation and trace metal data, these $\delta^{15}\text{N}_{\text{sed}}$ values imply redox stratification during deposition of the Miaohe Member. In a stratified water-column, nitrate is depleted by assimilation in the upper mixed layer and subsequently denitrified at the redox transition zone, below which ammonia accumulates and is quantitatively converted to N_2 or N_2O by coupled nitrification, denitrification and anammox (Ader et al., 2014). Because of the different processes operating vertically in a stratified water mass, sedimentary nitrogen isotope values relate to the positioning of the intermediate redox transition zone. Typically, $\delta^{15}\text{N}_{\text{sed}}$ values of $\sim 0\text{‰}$ can be expected in this setting due to nitrate limitation and productivity fuelled by N_2 -fixation (Quan & Falkowski, 2009). Instead, $\delta^{15}\text{N}_{\text{sed}}$ values of between 1.5‰ and 4‰ are recorded, implying partial nitrate availability and ‘normal’ productivity. Additionally, a source of nitrate is necessary to sustain euxinia, and inferred nitrate availability during deposition of the Miaohe Member at Miaohe is consistent with the Fe speciation data from Li et al. (2015) and trace metal enrichments observed in this study. At Miaohe, it is possible that surface water carried nitrate from the open ocean across the sill of the otherwise restricted basin, thereby reducing the influence of N_2 -fixation on $\delta^{15}\text{N}_{\text{sed}}$ values. Regardless, basin restriction would have still resulted in a nitrate-limited environment, with loss due to denitrification and assimilation. This is largely consistent with the hypothesis put forward by Kikumoto et al. (2014), where steadily decreasing $\delta^{15}\text{N}_{\text{sed}}$ values upwards through the Doushantuo Formation are thought to be the result of oxygenation of the global ocean, oxidation of a dissolved organic carbon pool and a gradual increase in the nitrate reservoir. Evidence for this is also provided in the form of Mo and V concentrations (Scott et al., 2008; Sahoo et al., 2016; Och et al., 2016) and $\delta^{34}\text{S}_{\text{py}}$, $\delta^{98}\text{Mo}$ and $\delta^{238}\text{U}$ data (McFadden et al., 2008; Kendall et al., 2015; Chen et al., 2015; Sahoo et al., 2016; Och et al., 2016; Wei et al., 2018; Ostrander et al., 2019).

Nitrogen isotope data are also available for the Jiuqunao, Jiulongwan and the drillcore correlative sites (Och et al., 2016; Kikumoto et al., 2014). For DST IV, $\delta^{15}\text{N}_{\text{sed}}$ values at Jiulongwan are stable at $\sim 4\text{‰}$, while those at the drillcore site are broadly similar to $\delta^{15}\text{N}_{\text{sed}}$ data from Miaohe ($2.3\text{‰} < \delta^{15}\text{N}_{\text{sed}} < 4.2\text{‰}$). A similar depositional setting to Miaohe can therefore be inferred, characterised by water-column stratification, partial nitrate availability and ‘normal’ productivity. Lower values are found at Jiuqunao ($0.5\text{‰} < \delta^{15}\text{N}_{\text{sed}} < 2.5\text{‰}$), implying nitrate-limitation and productivity fuelled by nitrogen fixation. Because of the close proximity of these sites, the different $\delta^{15}\text{N}_{\text{sed}}$ values indicate a structurally complex depositional basin, with isotopic nitrogen values relating to (1) sill depth and (2) access to the open ocean and dissolved nitrate inventory.

6.c. Paleogeographic control on local redox conditions

As previously mentioned, the Miaohe Member at Miaohe and Jiuqunao, and DST IV at Jiulongwan are thought to have been deposited in an intra-shelf lagoon environment (Vernhet & Reijmer, 2010; Jiang et al., 2011; Zhu et al., 2013). In this setting, intra-basinal water-column redox conditions would have related strongly to sill depth and communication with the open ocean. The trace metal/TOC proxy data examined in this study can be compared with data from modern anoxic systems to provide an insight into basin restriction and the paleogeographic controls on redox conditions. For the Black Sea, typical renewal times and Mo/TOC values are c. 400-800 years and ~4.5 respectively, while those for the Framvaren Fjord are c. 100-125 years and ~9 respectively (Algeo & Rowe, 2012). Trace metal/TOC proxy values for the Miaohe Member are lower than those of the Black Sea, therefore implying basin restriction and limited communication generally during deposition, however two discrete trace metal/TOC ‘zones’ can also be discerned (Fig. 5): (1) a period of moderate restriction from 2-12 m stratigraphic height (e.g. $0.27 < \text{Mo/TOC} < 1.40$; $0.90 < \text{U/TOC} < 3.46$) and (2) a period of extensive restriction from 12-23 m stratigraphic height (e.g. $0.35 < \text{Mo/TOC} < 1.01$; $0.61 < \text{U/TOC} < 2.08$). The section of the Miaohe Member from 12-23 m also records high $\text{Fe}_{\text{py}}/\text{Fe}_{\text{HR}}$ values and strong Mo, U, V and Cr enrichments, indicating that deposition of this unit occurred in a restricted basin characterised by poor ventilation, euxinia and extended water renewal times. Lastly, an abrupt increase in Mo/TOC, U/TOC and V/TOC values coincident with a lithological change from shale to dolostone occurs between 23-25 m stratigraphic height (Fig. 5).

Isotope data, including $\delta^{34}\text{S}_{\text{py}}$, $\delta^{98}\text{Mo}$ and $\delta^{238}\text{U}$ indicate widespread oxygenation during the late Ediacaran (McFadden et al., 2008; Kendall et al., 2015; Chen et al., 2015; Sahoo et al., 2016; Och et al., 2016; Wei et al., 2018; Ostrander et al., 2019). Redox conditions during deposition of the Miaohe Member and DST IV can therefore be attributed to local basin configuration and restriction as indicated by trace metal/TOC proxy data. Several authors (e.g. Li et al., 2015; Och et al., 2016; Bowyer et al., 2017) discuss the importance of partially conflicting redox data despite the acute geographical proximity of several of the intra-basinal study sites. Building on the ‘sulphidic-wedge’ model proposed by Li et al. (2010), Och et al. (2016) and Bowyer et al. (2017) propose a scenario where local redox conditions would have related to the movement of a stratified euxinic wedge over subsequent silled basins due to eustatic sea level change. In this setting, the sustained trace metal enrichment and $\delta^{15}\text{N}_{\text{sed}}$ levels at Miaohe can be explained by surface water flow across the sill from the open ocean, where redox-sensitive trace metals were likely abundant. Communication with a largely oxygenated open ocean would have also provided a mechanism for infiltration by the low-diversity Miaohe Biota assemblage, the preservation of which at ~7 m stratigraphic height implies sporadic oxygenation and eustatic change, albeit in a generally oxygen stressed environment. Although sedimentary trace metal enrichments and sustained euxinia at Jiulongwan (Li et al., 2010) similarly indicate access to the open ocean, low Mo enrichments (Li et al., 2015; Och et al., 2016) and lower $\delta^{15}\text{N}_{\text{sed}}$ values (Och et al., 2016) at Jiuqunao imply sustained restriction and limited access to the open ocean nitrate and redox-sensitive

trace metal inventories. Because of the close proximity of these sites, considerable basin complexity can be inferred.

To summarise, eustatic sea level change would have controlled communication between the structurally-complex intra-shelf basin and the open ocean. During a period of eustatic sea level rise, increased nitrate availability would have fuelled productivity, enabling the development of euxinic bottom water. In this setting, trace metals from the open ocean would have been easily scavenged and sequestered by Miaohe Member sediments. At more proximal locations, access to the open ocean was reduced, euxinia was inhibited and trace metals were not easily scavenged.

6.d. Paleoredox and evolution of the Miaohe Biota

Molecular evidence points to the emergence of complex metazoans, including crown-group demosponges and cnidarians prior to deposition of the Miaohe Member (Erwin et al., 2011). Despite this, the Miaohe Biota comprises a simple, low-diversity assemblage. This lack of complexity is likely the result of quasi-continuous anoxic-stress within the intra-shelf lagoon environment; however, nutrient availability, water energy and temperature fluctuations could have also contributed (Li et al., 2015). In this restricted setting, periodic access to the open ocean could have provided partial relief from these stresses, enabling simple metazoan communities to persist. This is consistent with their occurrence during a period of inferred eustatic sea level rise. As previously noted by Li et al. (2015), the Miaohe Biota colonisation is linked to spatially variable redox patterns. At Jiulongwan and in the overlying Miaohe Member at Miaohe, euxinia and toxic stress would have inhibited metazoan colonisation, while the absence of the Miaohe Biota at Jiuqunao is likely due to isolation from the open ocean. If continental margins at other locations globally were similarly redox-stressed, then the late Ediacaran could represent a period of suppressed evolution.

7. Conclusions

The ‘Miaohe Member’ has previously been partially correlated with DST IV (Xiao et al., 2017; Zhou et al., 2017) or with the younger Shibantan Member of the Dengying Formation (An et al., 2015). New Miaohe Member $\delta^{13}\text{C}$ data from Miaohe and Jiuqunao are remarkably similar to $\delta^{13}\text{C}$ data from DST IV at Jiulongwan and partial correlation with DST IV at Jiulongwan can therefore be inferred. Although Zhou et al. (2017) and Xiao et al. (2017) consider the sum of the LBS, intermediate dolostone and Miaohe Member to correlate with DST IV, it is likely that the LBS represents a portion of the Miaohe Member that has acted as a slip surface, carrying deformed dolostones of the Hamajing Member – the intermediate dolostone. This interpretation appears to be the most parsimonious explanation for the lack of such units, or related isotopic complexity at the relatively undisturbed Jiulongwan section in the east.

New $\text{Fe}_{\text{HR}}/\text{Fe}_{\text{T}}$ data from the Miaohe Member at Miaohe is indicative of sustained anoxia, while patterns of redox-sensitive trace metal enrichment imply water-column euxinia during deposition of the uppermost Miaohe Member shales. Miaohe Biota-associated and over/underlying shales record limited relative Mo enrichment and were likely deposited in a predominantly anoxic but non-euxinic setting. These conclusions are largely supported by $\text{Fe}_{\text{py}}/\text{Fe}_{\text{HR}}$ data from Li et al. (2015). Secondary oxidative weathering and Fe_{py} depletion is recorded by the samples obtained for this study, and $\text{Fe}_{\text{py}}/\text{Fe}_{\text{HR}}$ ratios cannot therefore be interpreted.

Trace metal/TOC proxy values indicate that the Miaohe Member at Miaohe was deposited in a water-column characterised by restriction and limited renewal. Despite this, sustained trace metal concentrations and $\delta^{15}\text{N}_{\text{sed}}$ values imply at least partial access to open ocean inventories. As discussed in Och et al. (2016) and Bowyer et al. (2017), it is likely that communication with the open ocean at Miaohe, Jiuqunao, Jiulongwan and other intrashelf basin sites was controlled by a sill; during periods of eustatic sea level rise, nitrate and trace metal inventories would have been replenished, thereby facilitating the development of euxinic bottom water. The intrashelf basin was also likely characterised by significant structural complexity, with limited communication between sites. At more proximal locations such as Jiuqunao, access to the open ocean would have been reduced, inhibiting water-column euxinia. This environmental stress could have influenced Ediacaran metazoan development in southern China and other similar sites globally.

8. Acknowledgements

This work was supported by funding from the joint NERC-NSFC Biosphere Evolution Transitions and Resilience (BETR) programme (NE/P013643/1). SWP acknowledges support from a Royal Society Wolfson Research Merit Award. We would like to thank Gary Tarbuck and Dr Anne-Lise Jourdan (both UCL) for laboratory assistance.

9. References

- Ader M, Sansjofre P, Halverson GP, Busigny V, Trindade RIF, Kunzmann M and Nogueira ACR** (2014) Ocean redox structure across the Late Neoproterozoic Oxygenation Event: a nitrogen isotope perspective. *Earth and Planetary Science Letters* **396**, 1–13.
- Ahm ASC, Bjerrum CJ and Hammarlund, EU** (2017) Disentangling the record of diagenesis, local redox conditions, and global seawater chemistry during the latest Ordovician glaciation. *Earth and Planetary Science Letters* **459**, 145–56.
- Algeo TJ and Lyons TW** (2006) Mo-total organic carbon covariation in modern anoxic marine environments: implications for analysis of paleoredox and paleohydrographic conditions. *Paleoceanography* **21**, PA1016.
- Algeo TJ and Maynard JB** (2004) Trace-element behavior and redox facies in core shales of Upper Pennsylvanian Kansas-type cyclothems. *Chemical Geology* **206**, 289–318.
- Algeo TJ and Rowe H** (2012) Paleooceanographic applications of trace-metal concentration data. *Chemical Geology* **324–325**, 6–18.
- Algeo TJ and Tribovillard N** (2009) Environmental analysis of paleooceanographic systems based on molybdenum–uranium covariation. *Chemical Geology* **268**, 211–25.
- An Z, Jiang G, Tong J, Tian L, Ye Q, Song H and Song H** (2015) Stratigraphic position of the Ediacaran Miaohu biota and its constraints on the age of the upper Doushantuo $\delta^{13}\text{C}$ anomaly in the Yangtze Gorges area, South China. *Precambrian Research* **271**, 243–53.
- Anderson RF, Fleisher MQ and LeHuray AP** (1989) Concentration, oxidation state, and particulate flux of uranium in the Black Sea. *Geochimica et Cosmochimica Acta* **53**, 2215–24.
- Benkovitz A, Matthews A, Teutsch N, Poulton SW, Bar-Matthews M and Almogi-Labin A** (2020) Tracing water column euxinia in Eastern Mediterranean sapropels S5 and S7. *Chemical Geology* **545**, 119627.
- Bertine K and Turekian K** (1973) Molybdenum in marine deposits. *Geochimica et Cosmochimica Acta* **37**, 1415–34.
- Bowyer F, Wood RA and Poulton SW** (2017) Controls on the evolution of Ediacaran metazoan ecosystems: a redox perspective. *Geobiology* **15**, 516–51.
- Breit GN and Wanty RB** (1991) Vanadium accumulation in carbonaceous rocks: a review of geochemical controls during deposition and diagenesis. *Chemical Geology* **91**, 83–97.
- Broecker W and Peng T** (1982) Tracers in the Sea. *Eldigio Press*, Columbia University, Palisades, NY.
- Butterfield NJ** (2009) Oxygen, animals and oceanic ventilation: an alternative view. *Geobiology* **7**, 1–7.

- Calvert S and Pedersen T** (1993) Geochemistry of recent oxic and anoxic marine sediments: implications for the geological record. *Marine Geology* **113**, 67–88.
- Calvert SE and Piper DZ** (1984) Geochemistry of ferromanganese nodules from DOMES Site A, Northern Equatorial Pacific: multiple diagenetic metal sources in the deep sea. *Geochimica et Cosmochimica Acta* **48**, 1913–28.
- Canfield DE** (1989) Reactive iron in marine sediments. *Geochimica et Cosmochimica Acta* **53**, 619–32.
- Canfield DE, Poulton SW and Narbonne GM** (2007) Late-Neoproterozoic deep-ocean oxygenation and the rise of animal life. *Science* **315**, 92–5.
- Canfield DE, Poulton SW, Knoll AH, Narbonne GM, Ross G, Goldberg T and Strauss H** (2008) Ferruginous conditions dominated later Neoproterozoic deep-water chemistry. *Science* **321**, 949–52.
- Canfield DE, Raiswell R, Westrich JT, Reaves CM and Berner RA** (1986) The use of chromium reduction in the analysis of reduced inorganic sulfur in sediments and shales. *Chemical Geology* **54**, 149–55.
- Chen X, Ling H-F, Vance D, Shields-Zhou GA, Zhu M, Poulton SW, Och LM, Jiang S-Y, Li D, Cremonese L and Archer C** (2015) Rise to modern levels of ocean oxygenation coincided with the Cambrian radiation of animals. *Nature Communications* **6**, 7142.
- Chen M and Xiao Z** (1992) Macrofossil biota from upper Doushantuo Formation in eastern Yangtze Gorges, China. *Acta Palaeontologica Sinica* **31**, 513–29.
- Clarkson MO, Poulton SW, Guilbaud R and Wood RA** (2014) Assessing the utility of Fe/Al and Fe-speciation to record water column redox conditions in carbonate-rich sediment. *Chemical Geology* **382**, 111–22
- Condon D, Zhu M, Bowring S, Wang W, Yang A and Jin Y** (2005) U-Pb ages from the Neoproterozoic Doushantuo Formation, China. *Science* **308**, 95–8.
- Cranston RE and Murray JW** (1978) The determination of chromium species in natural waters. *Analytica Chimica Acta* **99**, 275–82.
- Cremonese L, Shields-Zhou G, Struck U, Ling H-F, Och L, Chen X and Li D** (2013) Marine biogeochemical cycling during the early Cambrian constrained by a nitrogen and organic carbon isotope study of the Xiaotan section, South China. *Precambrian Research* **225**, 148–65.
- Crusius J, Calvert S, Pedersen T and Sage D** (1996) Rhenium and molybdenum enrichments in sediments as indicators of oxic, suboxic and sulfidic conditions of deposition. *Earth and Planetary Science Letters* **145**, 65–78.

- Ding L, Li Y, Hu X, Xiao Y, Su C and Huang J** (1996) Sinian Miaohu biota. *Geological Publishing House*, Beijing, 1–221.
- Elderfield H** (1970) Chromium speciation in sea water. *Earth and Planetary Science Letters* **9**, 10–6.
- Emerson S, Cranston RE and Liss PS** (1979) Redox species in a reducing fjord: equilibrium and kinetic considerations. *Deep Sea Research Part A. Oceanographic Research Papers* **26**, 859–78.
- Emerson SR and Husted SS** (1991) Ocean anoxia and the concentrations of molybdenum and vanadium in seawater. *Marine Chemistry* **34**, 177–96.
- Erickson BE and Helz GR** (2000) Molybdenum(VI) speciation in sulfidic waters. *Geochimica et Cosmochimica Acta* **64**, 1149–58.
- Erwin DH, Laflamme M, Tweedt SM, Sperling EA, Pisani D and Peterson KJ** (2011) The Cambrian Conundrum: Early Divergence and Later Ecological Success in the Early History of Animals. *Science* **334**, 1091–1097.
- Fike DA, Grotzinger JP, Pratt LM and Summons RE** (2006) Oxidation of the Ediacaran ocean. *Nature* **444**, 744–7.
- Goldberg T, Archer C, Vance D, Thamdrup B, McAnena A and Poulton SW** (2012) Controls on Mo isotope fractionations in a Mn-rich anoxic marine sediment, Gullmar Fjord, Sweden. *Chemical Geology* **296–297**, 73–82.
- Helz GR, Bura-Nakić E, Mikac N and Ciglenečki I** (2011) New model for molybdenum behavior in euxinic waters. *Chemical Geology* **284**, 323–32.
- Helz GR, Miller CV, Charnock JM, Mosselmans JFW, Pattrick RAD, Garner CD and Vaughan DJ** (1996) Mechanism of molybdenum removal from the sea and its concentration in black shales: EXAFS evidence. *Geochimica et Cosmochimica Acta* **60**, 3631–42.
- Huerta-Diaz MA and Morse JW** (1992) Pyritization of trace metals in anoxic marine sediments. *Geochimica et Cosmochimica Acta* **56**, 2681–702.
- Jiang G, Kaufman AJ, Christie-Blick N, Zhang S and Wu H** (2007) Carbon isotope variability across the Ediacaran Yangtze Platform in South China: implications for a large surface-to-deep ocean $\delta^{13}\text{C}$ gradient. *Earth and Planetary Science Letters* **261**, 303–20.
- Jiang G, Kennedy MJ, Christie-Blick N, Wu H and Zhang S** (2006) Stratigraphy, sedimentary structures, and textures of the Late Neoproterozoic Doushantuo cap carbonate in South China. *Journal of Sedimentary Research* **76**, 978–95.
- Jiang G, Shi X, Zhang S, Wang Y and Xiao S** (2011) Stratigraphy and paleogeography of the Ediacaran Doushantuo Formation (ca. 635–551Ma) in South China. *Gondwana Research* **19**, 831–49.

- Jiang G, Sohl LE and Christie-Blick N** (2003) Neoproterozoic stratigraphic comparison of the Lesser Himalaya (India) and Yangtze block (south China): paleogeographic implications. *Geology* **31**, 917.
- Kendall B, Komiya T, Lyons TW, Bates SM, Gordon GW, Romaniello SJ, Jiang G, Creaser RA, Xiao S, McFadden K, Sawaki Y, Tahata M, Shu D, Han J, Li Y, Chu X and Anbar AD** (2015) Uranium and molybdenum isotope evidence for an episode of widespread ocean oxygenation during the late Ediacaran Period. *Geochimica et Cosmochimica Acta* **156**, 173–93.
- Kikumoto R, Tahata M, Nishizawa M, Sawaki Y, Maruyama S, Shu D, Han J, Komiya T, Takai K and Ueno Y** (2014) Nitrogen isotope chemostratigraphy of the Ediacaran and Early Cambrian platform sequence at Three Gorges, South China. *Gondwana Research* **25**, 1057–69.
- Klinkhammer G and Palmer M** (1991) Uranium in the oceans: where it goes and why. *Geochimica et Cosmochimica Acta* **55**, 1799–806.
- Langmuir D** (1978) Uranium solution-mineral equilibria at low temperatures with applications to sedimentary ore deposits. *Geochimica et Cosmochimica Acta* **42**, 547–69.
- Li C, Hardisty DS, Luo G, Huang J, Algeo TJ, Cheng M, Shi W, An Z, Tong J, Xie S, Jiao N and Lyons TW** (2017) Uncovering the spatial heterogeneity of Ediacaran carbon cycling. *Geobiology* **15**, 211–24.
- Li C, Love GD, Lyons TW, Fike DA, Sessions AL and Chu X** (2010) A stratified redox model for the Ediacaran ocean. *Science* **328**, 80–3.
- Li C, Planavsky NJ, Shi W, Zhang Z, Zhou C, Cheng M, Tarhan LG, Luo G and Xie S** 2015. Ediacaran marine redox heterogeneity and early animal ecosystems. *Scientific Reports* **5**, 17097.
- Lu M, Zhu M, Zhang J, Shields-Zhou G, Li G, Zhao F, Zhao X and Zhao M** (2013) The DOUNCE event at the top of the Ediacaran Doushantuo Formation, South China: broad stratigraphic occurrence and non-diagenetic origin. *Precambrian Research* **225**, 86–109.
- Lyons TW, Anbar AD, Severmann S, Scott C and Gill B C** (2009) Tracking euxinia in the ancient ocean: a multiproxy perspective and Proterozoic case study. *Annual Review of Earth and Planetary Sciences* **37**, 507–34.
- McFadden KA, Huang J, Chu X, Jiang G, Kaufman AJ, Zhou C, Yuan X and Xiao S** (2008) Pulsed oxidation and biological evolution in the Ediacaran Doushantuo Formation. *Proceedings of the National Academy of Sciences of the United States of America* **105**, 3197–202.
- McLennan SM** (2001) Relationships between the trace element composition of sedimentary rocks and upper continental crust. *Geochemistry, Geophysics, Geosystems* **2**.

- McManus J, Berelson WM, Klinkhammer GP, Hammond DE and Holm C** (2005) Authigenic uranium: relationship to oxygen penetration depth and organic carbon rain. *Geochimica et Cosmochimica Acta* **69**, 95–108.
- Morford JL and Emerson S** (1999) The geochemistry of redox sensitive trace metals in sediments. *Geochimica et Cosmochimica Acta* **63**, 1735–50.
- Morse JW and Luther GW** (1999) Chemical influences on trace metal-sulfide interactions in anoxic sediments. *Geochimica et Cosmochimica Acta* **63**, 3373–8.
- Narbonne GM and Gehling JG** (2003) Life after snowball: the oldest complex Ediacaran fossils. *Geology* **31**, 27–30.
- Och LM, Cremonese L, Shields-Zhou GA, Poulton SW, Struck U, Ling H, Li D, Chen X, Manning C, Thirlwall M, Strauss H and Zhu M** (2016) Palaeoceanographic controls on spatial redox distribution over the Yangtze Platform during the Ediacaran–Cambrian transition. *Sedimentology* **63**, 378–410.
- Ostrander CM, Sahoo SK, Kendall B, Jiang G, Planavsky NJ, Lyons TW, Nielsen SG, Owens JD, Gordon GW, Romaniello SJ and Anbar AD** (2019) Multiple negative molybdenum isotope excursions in the Doushantuo Formation (South China) fingerprint complex redox-related processes in the Ediacaran Nanhua Basin. *Geochimica et Cosmochimica Acta* **261**, 191–209.
- Poulton Brucker RL, McManus J and Poulton SW** (2012) Molybdenum isotope fractionations observed under anoxic experimental conditions. *Geochemical Journal* **46**, 201–9.
- Poulton SW** (2021) The iron speciation paleoredox proxy. *Geochemical Tracers in Earth System Science*, Cambridge University Press, in press.
- Poulton SW and Canfield DE** (2005) Development of a sequential extraction procedure for iron: implications for iron partitioning in continentally derived particulates. *Chemical Geology* **214**, 209–21.
- Poulton SW and Canfield DE** (2011) Ferruginous conditions: a dominant feature of the ocean through Earth's history. *Elements* **7**, 107–12.
- Poulton SW, Fralick PW and Canfield DE** (2004) The transition to a sulphidic ocean ~ 1.84 billion years ago. *Nature* **431**, 173–7.
- Poulton SW and Raiswell R** (2002) The low-temperature geochemical cycle of iron: from continental fluxes to marine sediment deposition. *American Journal of Science* **302**, 774–805.
- Qian Z, Zhensheng D and Xinzhi Z** (1995) Geochemical characteristics of Baiguoyuan black shale-type Ag-V deposit in Western Hubei Province. *Acta Mineralogica Sinica* **2**, 27–33.

- Quan TM and Falkowski PG** (2009) Redox control of N:P ratios in aquatic ecosystems. *Geobiology* **7**, 124–39.
- Quan TM, van de Schootbrugge B, Field MP, Rosenthal Y and Falkowski PG** (2008) Nitrogen isotope and trace metal analyses from the Mingolsheim core (Germany): evidence for redox variations across the Triassic-Jurassic boundary. *Global Biogeochemical Cycles* **22**, 1-14.
- Raiswell R and Canfield DE** (1996) Rates of reaction between silicate iron and dissolved sulfide in Peru Margin sediments. *Geochimica et Cosmochimica Acta* **60**, 2777–87.
- Raiswell R and Canfield DE** (1998) Sources of iron for pyrite formation in marine sediments. *American Journal of Science* **298**, 219–45.
- Raiswell R, Canfield DE and Berner RA** (1994) A comparison of iron extraction methods for the determination of degree of pyritisation and the recognition of iron-limited pyrite formation. *Chemical Geology* **111**, 101–10.
- Raiswell R, Hardisty DS, Lyons TW, Canfield DE, Owens JD, Planavsky NJ, Poulton SW and Reinhard CT** (2018) The iron paleoredox proxies: a guide to the pitfalls, problems and proper practice. *American Journal of Science* **318**, 491–526.
- Raiswell R, Newton R and Wignall PB** (2001) An indicator of water-column anoxia: resolution of biofacies variations in the Kimmeridge Clay (Upper Jurassic, U.K.). *Journal of Sedimentary Research* **71**, 286–94.
- Sahoo SK, Planavsky NJ, Jiang G, Kendall B, Owens JD, Wang X, Shi X, Anbar AD and Lyons TW** (2016) Oceanic oxygenation events in the anoxic Ediacaran ocean. *Geobiology* **14**, 457–68.
- Schmitz M** (2012). Appendix 2 – Radiometric ages used in GTS2012. In *The Geological Time Scale 2012* (eds F Gradstein, J Ogg, M Schmitz and G Ogg), pp.1045–82. Elsevier, Boston.
- Scott C, Lyons TW, Bekker A, Shen Y, Poulton SW, Chu X and Anbar AD** (2008) Tracing the stepwise oxygenation of the Proterozoic ocean. *Nature* **452**, 456–9.
- Shen Y, Canfield DE and Knoll AH** (2002) Middle Proterozoic ocean chemistry: evidence from the McArthur Basin, northern Australia. *American Journal of Science* **302**, 81–109.
- Shen Y, Knoll AH and Walter MR** (2003) Evidence for low sulphate and anoxia in a mid-Proterozoic marine basin. *Nature* **423**, 632–5.
- Shi W, Li C, Luo G, Huang J, Algeo TJ, Jin C, Zhang Z and Cheng M** (2018) Sulfur isotope evidence for transient marine-shelf oxidation during the Ediacaran Shuram Excursion. *Geology* **46**, 267–70.

- Shields GA, Mills BJW, Zhu M, Raub TD, Daines SJ and Lenton TM** (2019) Unique Neoproterozoic carbon isotope excursions sustained by coupled evaporite dissolution and pyrite burial. *Nature Geoscience* **12**, 823–7.
- Shields-Zhou G and Och L** (2011) The case for a Neoproterozoic Oxygenation Event: geochemical evidence and biological consequences. *GSA Today* **21**(3), 4–11.
- Sigman DM, Karsh KL and Casciotti KL** (2009) Nitrogen isotopes in the ocean. In *Encyclopedia of Ocean Sciences* (eds J Steele, S Thorpe and K Turekian), pp. 40–54. Elsevier.
- Sperling EA, Halverson GP, Knoll AH, MacDonald FA and Johnston DT** (2013) A basin redox transect at the dawn of animal life. *Earth and Planetary Science Letters* **371–372**, 143–55.
- Steiner M, Wallis E, Erdtmann B-D, Zhao Y and Yang R** (2001) Submarine-hydrothermal exhalative ore layers in black shales from South China and associated fossils — insights into a Lower Cambrian facies and bio-evolution. *Palaeogeography, Palaeoclimatology, Palaeoecology* **169**, 165–91.
- Tesdal J-E, Galbraith ED and Kienast M** (2013) Nitrogen isotopes in bulk marine sediment: linking seafloor observations with subseafloor records. *Biogeosciences* **10**, 101–18.
- Tostevin R, Clarkson MO, Gangl S, Shields GA, Wood RA, Bowyer F, Penny AM and Stirling CH** (2019) Uranium isotope evidence for an expansion of anoxia in terminal Ediacaran oceans. *Earth and Planetary Science Letters* **506**, 104–12.
- Tribovillard N, Algeo TJ, Lyons T and Riboulleau A** (2006) Trace metals as paleoredox and paleoproductivity proxies: an update. *Chemical Geology* **232**, 12–32.
- Tribovillard N, Riboulleau A, Lyons T and Baudin F** (2004) Enhanced trapping of molybdenum by sulfurized marine organic matter of marine origin in Mesozoic limestones and shales. *Chemical Geology* **213**, 385–401.
- Vernhet E, Heubeck C, Zhu M-Y and Zhang J-M** (2007) Stratigraphic reconstruction of the Ediacaran Yangtze Platform margin (Hunan province, China) using a large olistolith. *Palaeogeography, Palaeoclimatology, Palaeoecology* **254**, 123–39.
- Vernhet E and Reijmer JJG** (2010) Sedimentary evolution of the Ediacaran Yangtze Platform shelf (Hubei and Hunan provinces, Central China). *Sedimentary Geology* **225**, 99–115.
- Vorlicek TP, Kahn MD, Kasuya Y and Helz GR** (2004) Capture of molybdenum in pyrite-forming sediments: role of ligand-induced reduction by polysulfides. *Geochimica et Cosmochimica Acta* **68**, 547–56.
- Wallis E** (2006) The climatic and environmental history of the south Chinese Yangtze Platform during the Neoproterozoic and early Cambrian: hydrothermally active and salinity stratified epicontinental basins, a key for understanding the “Cambrian

Explosion"? PhD thesis, Technische Universität Berlin, Berlin, Germany. Published thesis.

Wang X, Erdtmann B-D, Chen X and Mao X (1998) Integrated sequence-, bio- and chemostratigraphy of the terminal Proterozoic to lowermost Cambrian 'black rock series' from central South China. *Episodes* **21**, 178–89.

Wang XQ, Shi XY, Jiang GQ and Tang DJ (2014) Organic carbon isotope gradient and ocean stratification across the late Ediacaran–early Cambrian Yangtze Platform. *Science China Earth Sciences* **57**, 919–29.

Wanty RB and Goldhaber MB (1992) Thermodynamics and kinetics of reactions involving vanadium in natural systems: accumulation of vanadium in sedimentary rocks. *Geochimica et Cosmochimica Acta* **56**, 1471–83.

Wedepohl KH (1971) Environmental influences on the chemical composition of shales and clays. *Physics and Chemistry of the Earth* **8**, 307–33.

Wedepohl KH (1991) The composition of the upper Earth's crust and the natural cycles of selected metals. In *Metals and their compound in the environment: occurrence, analysis and biological relevance* (eds E Merian), pp. 3–17. Weinheim: VCH-Verlagsgesellschaft.

Wehrli B and Stumm W (1989) Vanadyl in natural waters: adsorption and hydrolysis promote oxygenation. *Geochimica et Cosmochimica Acta* **53**, 69–77.

Xiao S, Bykova N, Kovalick A and Gill BC (2017) Stable carbon isotopes of sedimentary kerogens and carbonaceous microfossils from the Ediacaran Miaohu Member in South China: implications for stratigraphic correlation and sources of sedimentary organic carbon. *Precambrian Research* **302**, 171–9.

Xiao S, Yuan X, Steiner M and Knoll AH (2002) Macroscopic carbonaceous compressions in a terminal Proterozoic shale: a systematic reassessment of the Miaohu biota, South China. *Journal of Paleontology* **76**, 347–76.

Zhang X, Sigman DM, Morel FMM and Kraepiel AML (2014) Nitrogen isotope fractionation by alternative nitrogenases and past ocean anoxia. *Proceedings of the National Academy of Sciences* **111**, 4782–87.

Zheng Y, Anderson RF, van Geen A and Kuwabara J (2000) Authigenic molybdenum formation in marine sediments: a link to pore water sulfide in the Santa Barbara Basin. *Geochimica et Cosmochimica Acta* **64**, 4165–78.

Zhou C and Xiao S (2007) Ediacaran $\delta^{13}\text{C}$ chemostratigraphy of South China. *Chemical Geology* **237**, 89–108.

Zhou C, Xiao S, Wang W, Guan C, Ouyang Q and Chen Z (2017) The stratigraphic complexity of the middle Ediacaran carbon isotopic record in the Yangtze Gorges area, South China, and its implications for the age and chemostratigraphic significance of the Shuram Excursion. *Precambrian Research* **288**, 23–38.

- Zhu W and Chen M** (1984) On the discovery of macrofossil algae from the late Sinian in the eastern Yangtze Gorges, South China. *Acta Botanica Sinica* **26**, 558-60.
- Zhu B, Jiang S, Pi D, Ge L and Yang J** (2018) Trace elements characteristics of black shales from the Ediacaran Doushantuo Formation, Hubei Province, South China: implications for redox and open vs. restricted basin conditions. *Journal of Earth Science* **29**, 342–52.
- Zhu M, Lu M, Zhang J, Zhao F, Li G, Aihua Y, Zhao X and Zhao M** (2013) Carbon isotope chemostratigraphy and sedimentary facies evolution of the Ediacaran Doushantuo Formation in western Hubei, South China. *Precambrian Research* **225**, 7–28.
- Zhu M, Zhang J, Steiner M, Yang A, Li G and Erdtmann B** (2003) Sinian-Cambrian stratigraphic framework for shallow- to deep-water environments of the Yangtze Platform: an integrated approach. *Progress in Natural Science* **13**, 951–60.
- Zhu M, Zhang J and Yang A** (2007) Integrated Ediacaran (Sinian) chronostratigraphy of South China. *Palaeogeography, Palaeoclimatology, Palaeoecology* **254**, 7–61.
- Zhuang H, Lu J, Fu J, Liu J, Ren C and Zou D** (1999) Evidence for transforming mineralization of Baiguoyuan silver-vanadium deposit hosted in black shale in Hubei, China. *Chinese Science Bulletin* **44**, 263-7.

Figure 1. (a) Paleoenvironmental map of the Yangtze Platform region in South China during deposition of Doushantuo Member IV (DST IV) – modified after Steiner et al. (2001) and Jiang et al. (2011). The red square indicates the location of Figure 1B. (b) Geological map of the southern portion of the Huangling anticline – modified after Xiao et al. (2017). The locations of sections examined in this study are indicated: (1) Miaohe, (2) Jiuqunao and (3) Jiulongwan. Vertical dashed lines divide the area into eastern, central and western zones as defined by Zhou et al. (2017). (c) Simplified stratigraphic columns for the Miaohe (this study; Li et al., 2015), Jiuqunao (Li et al., 2015) and Jiulongwan (Li et al., 2010) sections. Two stratigraphic correlations are proposed for the Miaohe, Jiuqunao and Jiulongwan sites: the ‘Z’ correlation (Zhou et al., 2017; Xiao et al., 2017) and the ‘A’ correlation (An et al., 2015). The location of the ash bed dated at 551.09 ± 1.02 Ma by Schmitz et al. (2012) is indicated, as is the location of the Miaohe Biota (Xiao et al., 2002).

Figure 2. Contrast between the least visibly weathered sample (A) and most visibly weathered sample (B). A was collected from the Miaohe Member at Miaohe at a stratigraphic height of 7.0 m and B was collected from the same section at 12.9 m.

Figure 3. Fe_{py}/Fe_{HR} vs. Fe_{ox}/Fe_{HR} cross-plot for samples from this study (solid black points) and Li et al. (2015) (white points). The high Fe_{ox}/Fe_{HR} and low Fe_{py}/Fe_{HR} values observed in samples from this study are indicative of modern weathering. Samples from Li et al. (2015) are more distributed, reflecting transient alteration.

Figure 4. Lithostratigraphy, $\delta^{13}C_{carb}$ and $\delta^{13}C_{carb}$ profiles for Miaohe, Jiuqunao (Western Zone), Jiulongwan and the drillcore site (Central Zone). The yellow zone indicates the correlation proposed in this study. UD, Upper Dolomite; LBS, Lower Black Shale; III, Doushantuo Member III; IV, Doushantuo Member IV. The location of the ash bed dated at 551.09 ± 1.02 Ma by Schmitz et al. (2012) is indicated, as is the location of the Miaohe Biota (Xiao et al., 2002).

Figure 5. Iron speciation, trace metal and $\delta^{15}N$ data from the Miaohe Member (M) section at Miaohe. Fe_{HR}/Fe_T values of <0.22 indicate deposition in an anoxic environment, while values of >0.38 suggest anoxia. Fe_{HR}/Fe_T values of 0.22-0.38 represent possible anoxia and should be interpreted with caution. Fe_{py}/Fe_{HR} data of <0.6 indicates deposition was in an anoxic-ferruginous setting, while values of >0.8 indicate euxinic conditions. Fe_{py}/Fe_{HR} values of 0.6-0.8 record possible euxinia and should be interpreted with caution. Abbreviations: Fe_T , total iron; Fe_{HR} , highly-reactive iron; Fe_{py} , iron pyrite; TOC, total organic carbon; DY, Dengying Formation; UD, Upper Dolostone. The location of the Miaohe Biota is indicated (Xiao et al., 2002).

Figure 6. Fe_{HR}/Fe_T vs. Fe_{py}/Fe_{HR} for this study (solid black points) and Li et al. (2015) (white points). Dotted red lines indicate thresholds: (1) an Fe_{HR}/Fe_T value of >0.38 indicates anoxia, while a value of >0.22 indicates possible anoxia; (2) an Fe_{py}/Fe_{HR} value of >0.8 indicates euxinia, while a value of >0.7 indicates possible euxinia and values of <0.7 indicate ferruginous conditions.

1 **Table 1.** Geochemical data for the studied ‘Miaohe Member samples from the Miaohe Section, South China.

2

Sample	Height (m)	TOC ^a (wt. %)	TN ^b (wt. %)	$\delta^{13}\text{C}_{\text{org}}$ (‰)	$\delta^{15}\text{N}$ (‰)	Mo EF ^c	V EF ^c	U EF ^c	Cr EF ^c	Mo/TOC (ppm/wt. %)	V/TOC (ppm/wt. %)	U/TOC (ppm/wt. %)	Fe _{carb} (wt. %)	Fe _{ox} (wt. %)	Fe _{mag} (wt. %)	Fe _{py} (wt. %)	Fe _{HR} ^d (wt. %)	Fe _T ^e (wt. %)	Fe _{HR} / Fe _T	Fe _{py} / Fe _{HR}
Miaohe Section																				
MR2	2	0.85	0.009	-38.19	2.41	4.29	1.44	2.96	2.35	0.91	21.71	1.16	0.01	0.32	0.04	0.003	0.37	0.57	0.65	0.009
MR2.5	2.5		0.016	-38.28	2.46	5.46	1.63	4.92	3.68				0.01	0.20	0.03	0.002	0.24	0.43	0.55	0.008
MR3	3	1.42	0.019	-38.07	3.47	2.20	1.73	3.07	2.62	0.48	26.94	1.25	0.01	0.09	0.01	0.001	0.10	0.22	0.46	0.009
MR5	5	0.89	0.039	-37.59	3.85	1.49	2.22	1.92	2.05	1.40	149.22	3.38	0.01	0.35	0.04	0.004	0.40	0.74	0.54	0.011
MR7	7	1.34	0.046	-37.89	3.15	1.00	1.76	1.73	1.73	0.84	105.90	2.73	0.01	0.28	0.03	0.003	0.32	0.63	0.51	0.009
MR7 FS	7.3	2.51	0.057	-37.89	3.50	0.89	2.50	1.58	2.39	0.27	54.27	0.90	0.03	0.29	0.02	0.006	0.35	0.68	0.51	0.016
M0.5	11.4	0.65	0.025	-36.93	2.19	2.30	2.77	3.75	3.07	1.14	97.83	3.46	0.02	0.77	0.09	0.003	0.88	1.11	0.79	0.003
M1	11.9	2.10	0.035	-37.52	2.32	3.26	3.16	5.92	3.23	0.35	24.04	1.18	0.01	0.23	0.03	0.004	0.27	0.42	0.65	0.013
M2	12.9	0.89	0.019	-37.40	2.76	3.76	2.16	4.31	2.43	0.79	32.29	1.69	0.04	0.41	0.02	0.019	0.48	0.59	0.82	0.039
M3.3	14.2	0.57	0.009	-37.21	3.28	5.47	2.16	3.95	2.63	0.75	21.21	1.02	0.02	0.17	0.01	0.000	0.21	0.28	0.73	0.000
M4.8	15.7	1.62	0.030	-37.37	2.21	3.69	2.93	5.00	3.48	0.54	30.78	1.38	0.01	0.35	0.04	0.002	0.40	0.55	0.73	0.006
MR5.8	16.7			-36.86	2.12	11.09	2.97	4.87	4.90				0.02	0.34	0.04	0.003	0.40	0.52	0.76	0.008
M6.3	17.2	0.67	0.008	-37.24	1.93	9.52	4.62	9.97	5.76	1.01	35.18	1.99	0.00	0.13	0.01	0.001	0.14	0.25	0.57	0.009
M7.3	18.2	0.49	0.008	-37.40	1.64	6.42	4.04	7.46	4.10	0.96	43.02	2.08	0.01	0.12	0.02	0.000	0.14	0.21	0.67	0.003
M8.8	19.7	0.46	0.006	-37.49	1.78	7.66	2.45	6.59	4.16	0.83	18.85	1.33	0.01	0.14	0.01	0.004	0.17	0.26	0.66	0.023
M10	20.9	1.26	0.022	-37.49	2.53	2.32	1.77	2.64	2.61	0.49	26.78	1.05	0.02	0.55	0.06	0.001	0.63	0.86	0.73	0.002
M11	21.9	2.69	0.043	-37.71	2.25	2.91	1.50	2.30	2.68	0.41	15.16	0.61	0.26	0.06	0.01	0.225	0.55	0.86	0.64	0.407
M12	22.9	2.33	0.034	-37.54	2.78	3.43	1.49	3.46	2.62	0.47	14.52	0.88	0.01	0.10	0.01		0.12	0.19		
M14	24.9	0.57	0.013	-36.72	2.46	2.72	2.30	3.64	2.39	1.11	66.65	2.75	0.00	0.64	0.08	0.033	0.75	0.81	0.81	0.217
M15.5	26.4	0.10	0.010	-34.82	2.77	5.06	1.38	3.03	1.83	9.20	178.50	10.30	0.02	0.43	0.05	0.023	0.52	0.75	0.91	0.031

3

^a TOC = Total organic carbon

^b TN = Total nitrogen

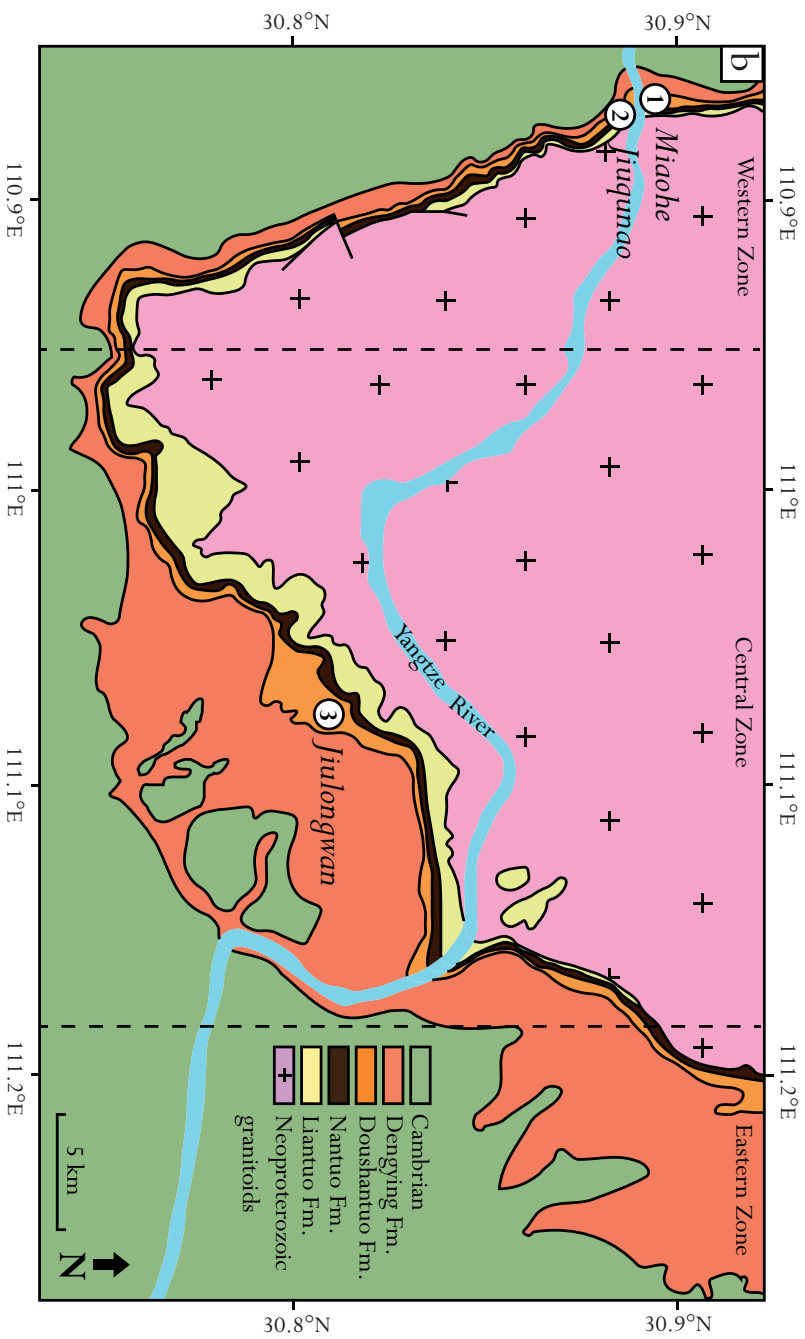
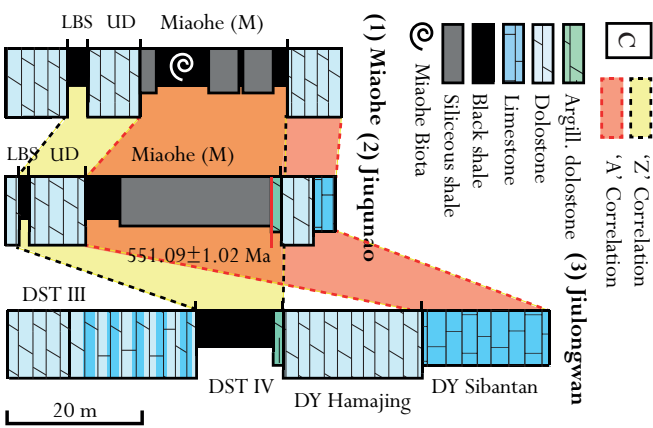
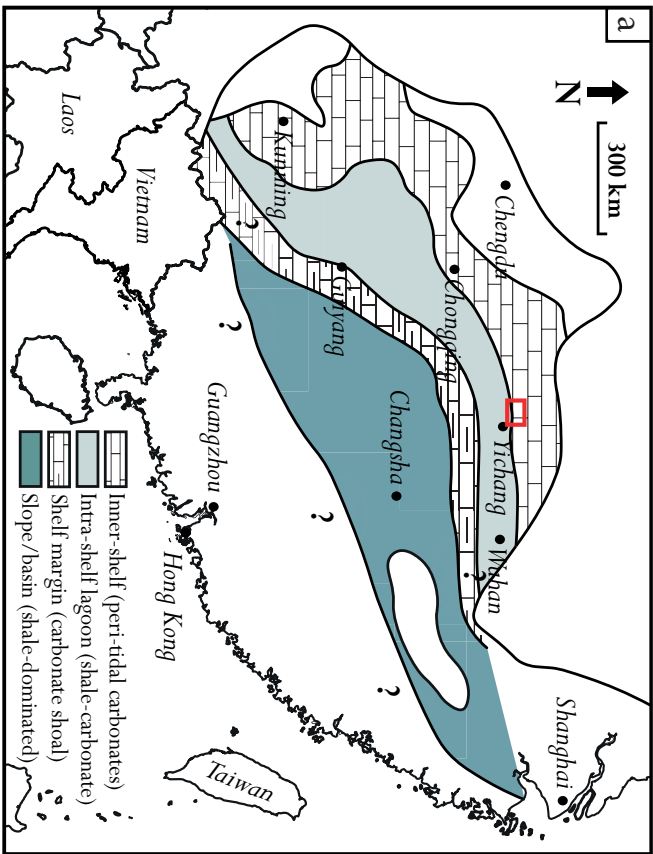
4

^c EF = Enrichment factor (normalised using upper continental crust values from McLennan (2001)).

^d Fe_{HR} = Highly-reactive iron pool (Fe_{carb}, Fe_{ox}, Fe_{mag} and Fe_{py})

5

^e Fe_T = Total Fe content

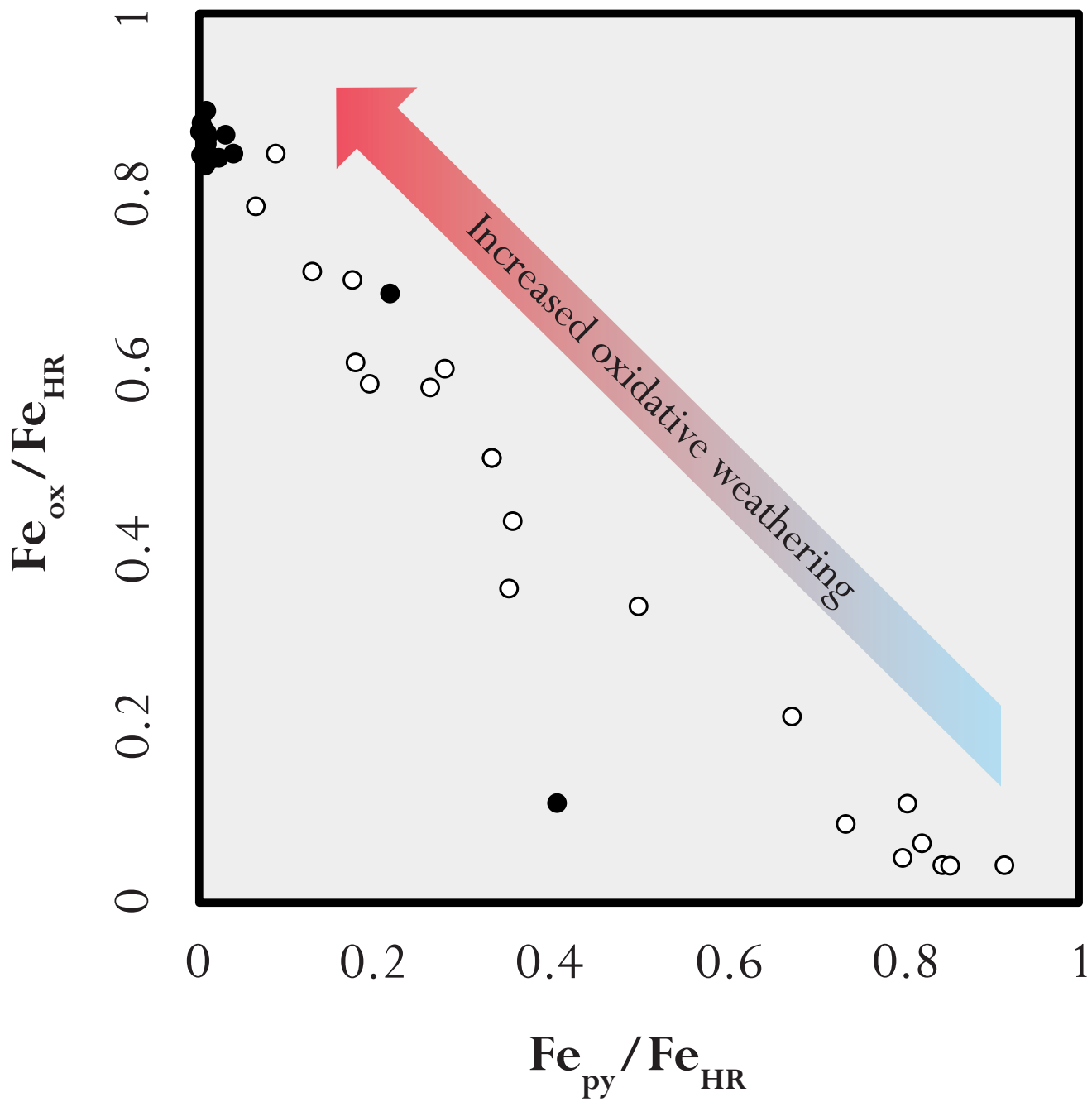


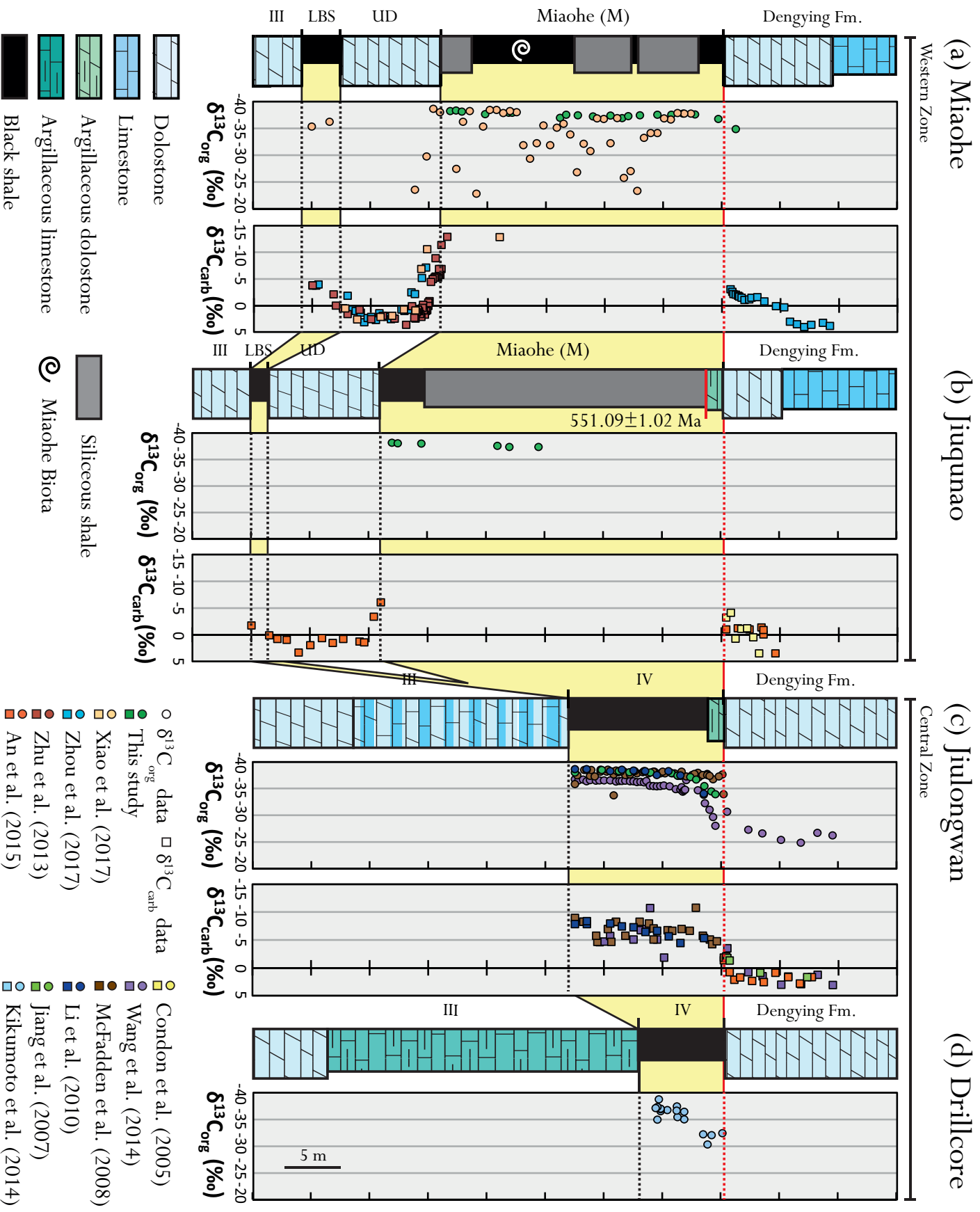
a

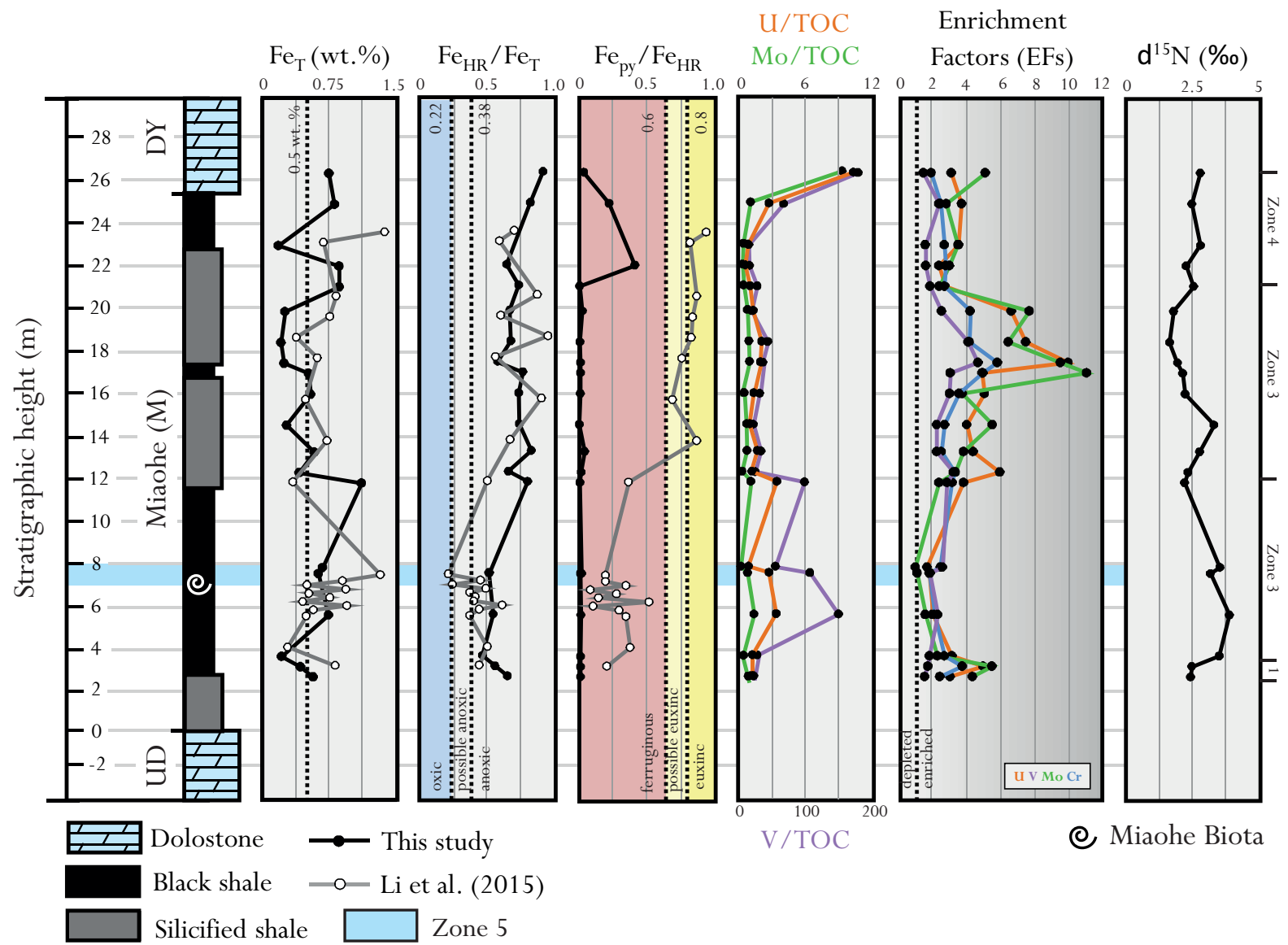


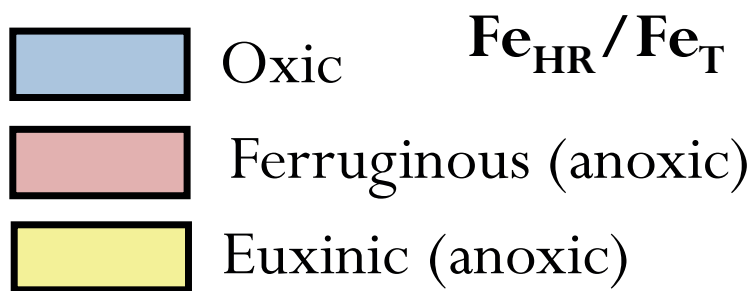
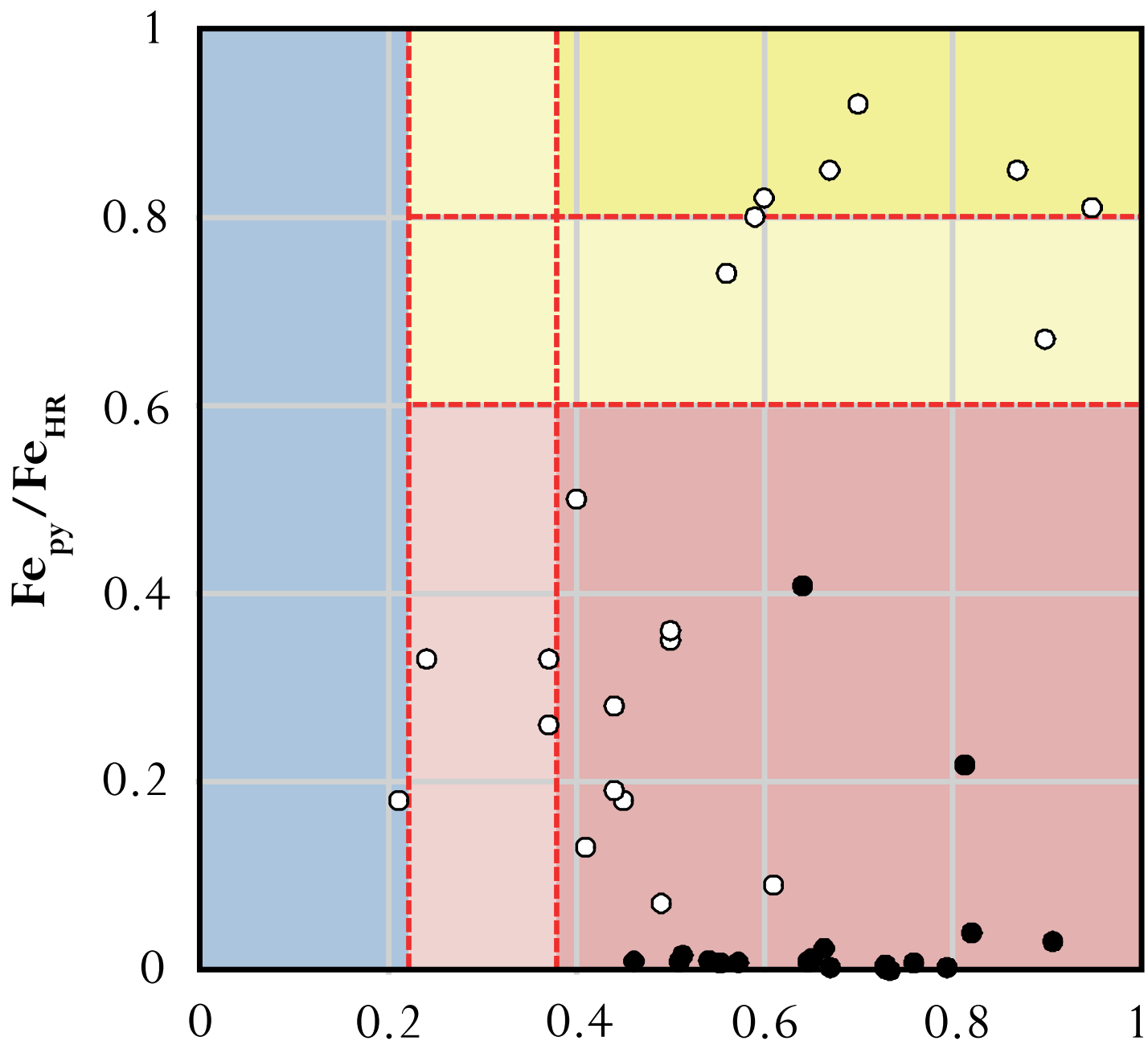
b











Supporting Online Material for

**The Ediacaran ‘Miaohe Member’ of South China: new insights
from paleoredox proxies and stable isotope data**

Paul Bridger*, Simon W. Poulton, Ying Zhou, Chao Li, Kun Zhang, Graham A. Shields


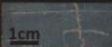







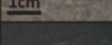









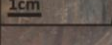

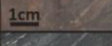



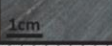








*To whom correspondence should be addressed. E-mail: pbr@bgs.ac.uk

This PDF includes:

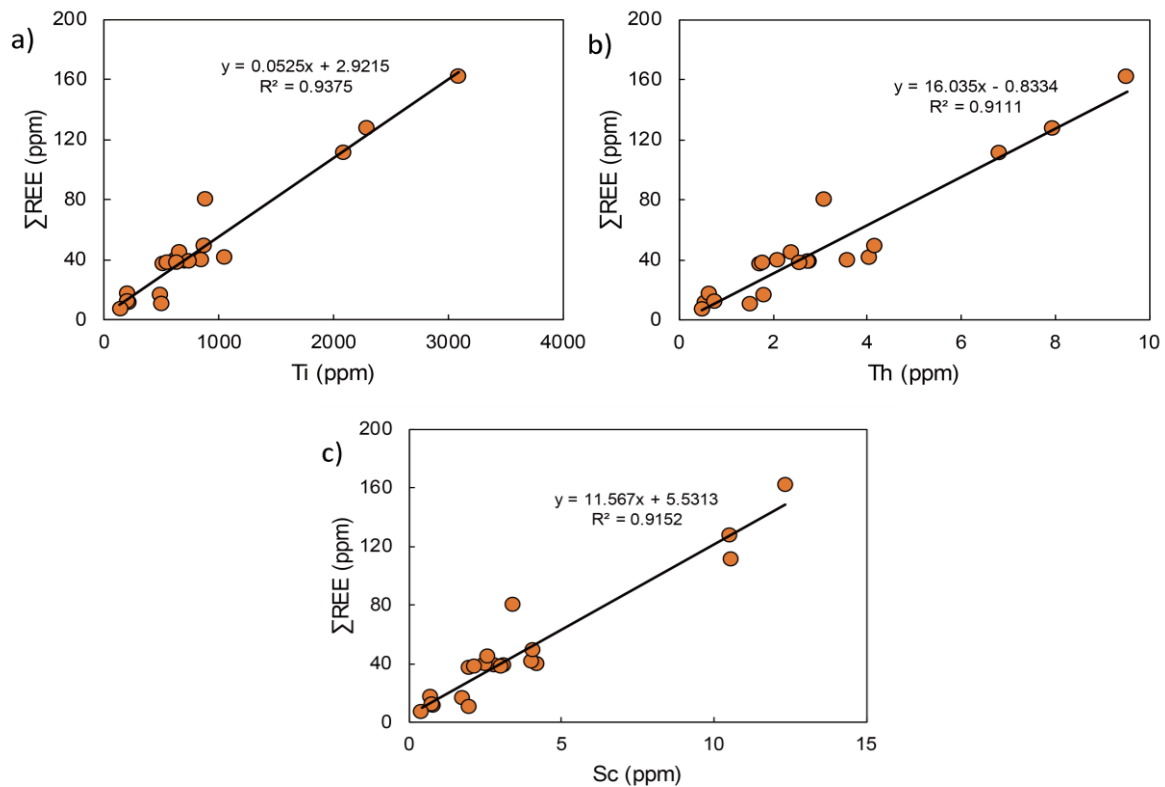
Figures S1-S5

Table S1

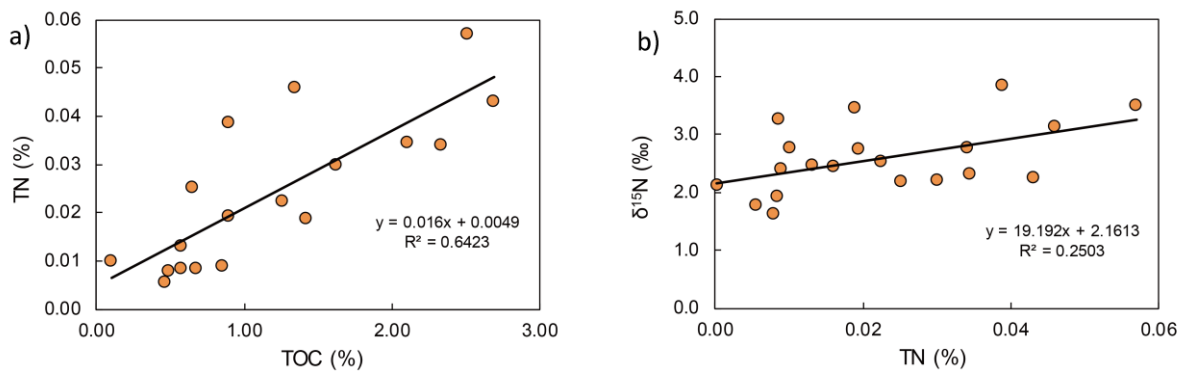
References

Sample	Height (m)	Weathered surface	Fresh surface	Colour	Weathered surface description	Lamination	Silicified	Other
MR2	2							
MR2.5	2.5				Red/orange oxidized surfaces	Very finely laminated	YES	Strongly indurated
MR3	3				Red/brown oxidized surfaces	Very finely laminated 0.05-0.1mm	YES	Strongly indurated
MR5	5				Yellow/orange/grey oxidized surfaces	Finely laminated 0.1-0.2mm	NO	Moderately indurated
MR7	7				Pink/brown oxidized surface	Not visible	NO	Moderately indurated
MR7 FS	7				Grey oxidized surface – limited weathering	Very finely laminated 0.05-0.2mm	NO	Moderately indurated
M0.5	11.4				Pink/brown oxidized surface	Very finely laminated 0.05-0.2mm	NO	Moderately indurated. Light-weight.
M1	11.9				Pale brown oxidized surfaces	Not visible	YES	Strongly indurated
M2	12.9				White, pink, brown oxidized surfaces.	Poorly laminated. Amorphous	YES	Strongly indurated. Conchoidal fracture
MR3.3	14.2							
M4.8	15.7				Some brown oxidation visible	Very finely laminated 0.2-0.5mm	YES	Strongly indurated
MR5.8	16.7				Brown/red oxidation visible	Finely laminated 0.5mm	NO	Moderately indurated. Heavily fractured/deformed
M6.3	17.2				Dark-brown oxidized surfaces	Finely laminated 1-2mm	YES	Strongly indurated
M7.3	18.2				Pale-brown oxidized surfaces	Not visible	YES	Strongly indurated. Conchoidal fracture
M8.8	19.7				Not visible	Not visible	YES	Strongly indurated. Amorphous nodules
M10	20.9				Strongly weathered, pitted surfaces. Pale brown to orange oxidation	Very finely laminated 0.2-0.5mm	YES	Strongly indurated
M11	21.9							
M12	22.9				Green/brown oxidized surfaces	Not visible	NO	Strongly indurated
M14	24.9				Not visible	Not visible	YES	Strongly indurated. Amorphous nodules
M15.5	26.4				Pale brown to white oxidation	Very finely laminated	NO	Strongly indurated. Calcareous. Crystalline

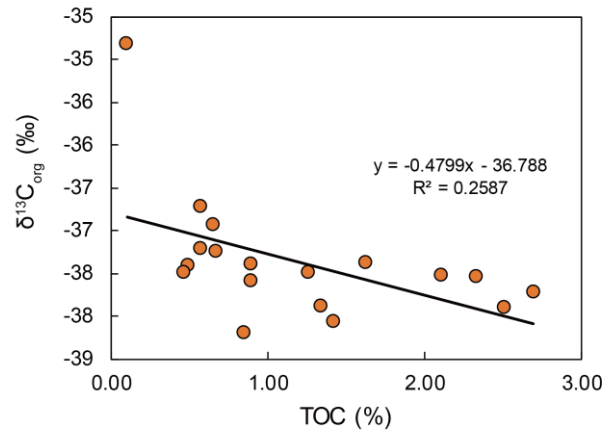
Supplementary Figure 1. Visual assessment of Miaohu Member samples



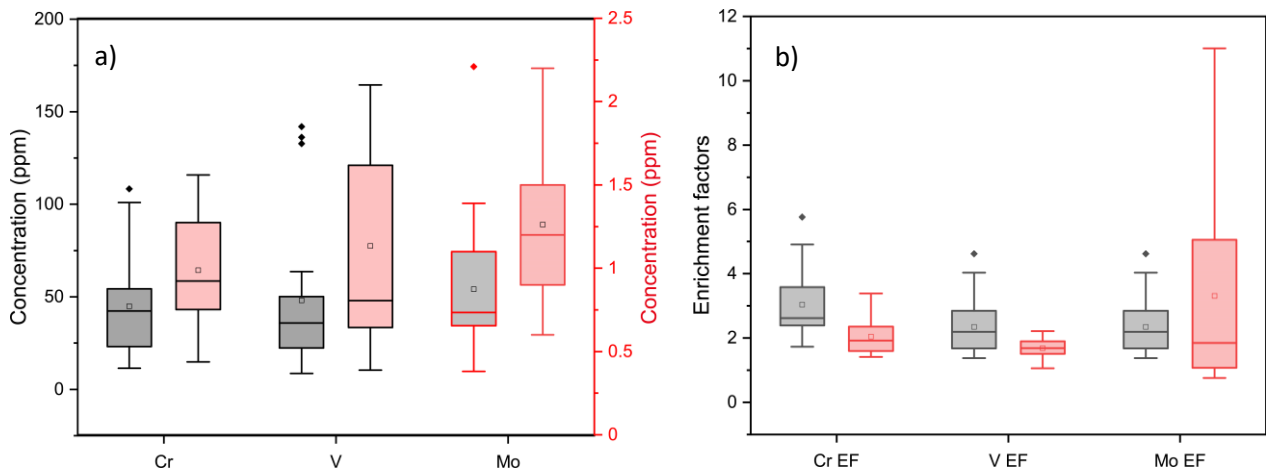
Supplementary Figure 2. Cross plots of Σ REE against (a) Ti, (b) Th and (c) Sc contents of the Miaohé Member shales from Miaohé.



Supplementary Figure 3. Cross plots of (a) TN vs. TOC and (b) $\delta^{15}\text{N}$ vs. TN for the Miaohé Member shales from Miaohé.



Supplementary Figure 4. Cross plot of $\delta^{13}\text{C}_{\text{org}}$ vs. TOC for the Miaohé Member shales at Miaohé.



Supplementary Figure 5. (a) Comparison of concentrations of redox-sensitive trace metals in highly weathered (grey box) and moderately weathered (pink box; Li et al., 2015) Miaohé Member shales from the Miaohé section. Note that the Mo concentrations with red borders correspond to the y-axis scale on the right-hand side. (b) Comparison of enrichment factors of redox-sensitive trace metals from highly weathered (grey box) and moderately weathered (pink box; Li et al., 2015) Miaohé Member shales from the Miaohé section.

Supplementary Table 1. Trace element concentrations for Miaohu Member samples from this study and Li et al. (2015)

Sample	Height (m)	U (ppm)	Mo (ppm)	Cr (ppm)	V (ppm)	Ti (ppm)
<i>This study</i>						
MR2	2	0.99	0.77	23.37	18.45	490.43
MR2.5	2.5	2.34	1.39	51.91	29.60	696.39
MR3	3	1.77	0.68	44.78	38.26	845.17
MR5	5	3.01	1.25	95.18	132.81	2291.26
MR7	7	3.66	1.13	108.30	141.91	3089.34
FS7.3/FS	7.3	2.26	0.68	101.00	136.21	2089.29
M0.5	11.4	2.25	0.74	54.66	63.59	878.40
M1	11.9	2.47	0.73	40.04	50.48	611.45
M2	12.9	1.50	0.70	25.08	28.74	509.27
M3.3	14.2	0.58	0.43	11.42	12.09	214.81
M4.8	15.7	2.23	0.88	46.01	49.86	652.42
M5.8	16.7	1.81	2.21	54.08	42.19	544.68
M6.3	17.2	1.33	0.68	22.79	23.57	195.34
M7.3	18.2	1.02	0.47	16.63	21.08	200.14
M8.8	19.7	0.61	0.38	11.41	8.67	135.58
M10	20.9	1.32	0.62	38.70	33.74	731.07
M11	21.9	1.64	1.11	56.72	40.77	1044.03
M12	22.9	2.05	1.09	45.98	33.83	867.76
M14	24.9	1.57	0.63	30.64	37.99	632.12
M15.5	26.4	1.03	0.92	18.37	17.85	497.12
<i>Li et al. (2015)</i>						
MH-23	23.5		0.9	44.53	47.72	1333.42
MH-22	23		1.8	43.10	40.55	973.36
MH-20	20.4		1.3	44.38	33.50	996.22
MH-19	19.4		1.1	35.91	31.80	1153.25
MH-18	18.4		1.1	36.68	30.39	770.48
MH-17	17.4		1.1	33.07	31.63	547.03
MH-15	15.4		1.5	23.54	26.84	476.57
MH-14	13.4		1.7	45.75	38.45	668.18
MH-13	11.4		1.4	14.80	10.46	347.57
MH-12	6.9		1.6	87.54	130.04	2992.31
MH-11	6.6		1.2	96.79	121.62	2675.08
MH-10	6.4		0.9	75.32	103.62	2634.17
MH-9	6.2		0.8	101.58	131.12	2491.33
MH-8	6		0.6	82.82	105.04	2155.39
MH-7	5.8		1	95.11	142.26	3230.67
MH-6	5.6		0.7	90.15	121.10	2406.31
MH-5	5.4		1.5	115.79	164.47	3787.80
MH-4	5.2		1.4	94.70	120.39	2432.33
MH-3	4.9		0.9	74.12	109.83	2295.94
MH-2	3.4		1.8	57.93	47.92	1047.48
MH-1	2.5		2.2	58.51	37.74	1169.31

References

LI, C., PLANAVSKY, N. J., SHI, W., ZHANG, Z., ZHOU, C., CHENG, M., TARHAN, L. G., LUO, G. & XIE, S. 2015. Ediacaran Marine Redox Heterogeneity and Early Animal Ecosystems. *Scientific Reports* **5**(1), 17097.